



# Crossing of Plasma Structures by spacecraft: a path calculator

Roberto Manuzzo, Gérard Belmont, Laurence Rezeau, F. Califano, R E Denton

## ► To cite this version:

Roberto Manuzzo, Gérard Belmont, Laurence Rezeau, F. Califano, R E Denton. Crossing of Plasma Structures by spacecraft: a path calculator. *Journal of Geophysical Research Space Physics*, 2019, 124 (12), pp.10119-10140. 10.1029/2019JA026632 . hal-02484704

**HAL Id: hal-02484704**

**<https://hal.science/hal-02484704>**

Submitted on 19 Feb 2020

**HAL** is a multi-disciplinary open access archive for the deposit and dissemination of scientific research documents, whether they are published or not. The documents may come from teaching and research institutions in France or abroad, or from public or private research centers.

L'archive ouverte pluridisciplinaire **HAL**, est destinée au dépôt et à la diffusion de documents scientifiques de niveau recherche, publiés ou non, émanant des établissements d'enseignement et de recherche français ou étrangers, des laboratoires publics ou privés.

# Crossing of Plasma Structures by spacecraft: a path calculator

R. Manuzzo<sup>1,2</sup>, G. Belmont<sup>1</sup>, L. Rezeau<sup>1</sup>, F. Califano<sup>2</sup>, R.E. Denton<sup>3</sup>

<sup>1</sup>LPP, CNRS, Ecole Polytechnique, Sorbonne Université, Univ. Paris-Sud, Observatoire de Paris,

Université Paris-Saclay, PSL Research University

<sup>2</sup>Department of Physics E. Fermi, Università di Pisa, Italia

<sup>3</sup>Department of Physics and Astronomy, Dartmouth College, Hanover, New Hampshire, USA

## Key Points:

- The Spatio-Temporal-Difference method is extended to determine non mono-dimensional spacecraft trajectories.
- Two new methods are developed for this determination: the Single and the Multi Variate Fit methods. They are compared to previous ones.
- A Gradient-Directed Monte Carlo approach is applied to optimize the results. The spacecraft path and magnetopause thickness are so computed.

---

Corresponding author: Laurence Rezeau, [laurence.rezeau@lpp.polytechnique.fr](mailto:laurence.rezeau@lpp.polytechnique.fr)

## Abstract

When spacecraft (*s/c*) missions probe plasma structures (*PS*) the relative location of the *s/c* with respect to the *PS* is unknown. This information is however needed to measure the geometrical features of the *PS* (orientation and thickness) and to understand the physical processes underlying the *PS* dynamics. Methods to determine the *s/c* location exist but they need strong assumptions to be satisfied (stationarity and special spatial dependencies). The number of cases for which these assumptions are likely to be valid for the entire *PS* seems to be limited and even weak departures from these hypothesis may affect the results. For a quasi-1D geometry in particular, the determination of the velocity component along the two quasi-invariant directions is very inaccurate and the assumption of strict stationarity may lead these quantities to diverge. In this paper we present new methods to compute the *s/c* trajectory through a *PS*, without *a priori* assumption on its spatial geometry, and able to work even in the presence of weak non-stationarities. The methods are tested both on artificial and real data, the latter provided by the Magnetospheric MultiScale (MMS) mission probing the Earth's magnetopause (*MP*). 1D and 2D trajectories of the MMS are found that can be used as an initial step for future reconstruction studies. Advanced minimization procedures to optimize the results are discussed.

## 1 Introduction

When spacecraft (*s/c*) cross plasma structures (*PSs*), the different parameters characterizing these structures are measured only as time series along the *s/c* trajectories. The shape and the motion of the *PSs* being unknown, it is quite difficult to determine both only from such temporal data. Multi-spacecraft missions like Cluster (Escoubet, Schmidt, & Goldstein, 1997) and the Magnetospheric MultiScale (MMS) (Burch, Moore, Torbert, & Giles, 2016b) have enabled considerable progress to determine the shape and motion of *PSs* since they make measurements at multiple locations, which helps to separate spatial and temporal variations. Nevertheless, in the general case of a complex geometrical shape for a *PS* and of a complex relative path of the *s/c* with respect to it, getting a full determination of the shape and motion of *PSs* remains challenging. Such determinations cannot be done, in general, without strong assumptions. But information about the shape and location of *PSs* is necessary for understanding the physical processes being studied. Regarding the Earth's Magnetopause (*MP*) for instance, which is the field and particle boundary between the shocked solar wind and the Earth's magnetosphere, one has to know first whether this boundary can be approximated by a 1D plane structure, as the simplest models assume, or not. If so, one only has to determine what is the direction of its normal and what is its global thickness (and the thickness of its different sub-structures if any (Rezeau, Belmont, Manuzzo, Aunai, & Dargent, 2018)). Actually, such a plane-like equilibrium is easily perturbed and it is rarely observed. Perturbations generally involve 2D and 3D variations, either due to inhomogeneities in the incident solar wind or to surface instabilities such as, for instance, Kelvin-Helmholtz (KH) or tearing instabilities. One has then to determine what are the shape and the dimensions of the vortices in the KH case (Faganello & Califano, 2017), or, in the case of reconnection, one has to determine the invariance directions, the shapes and dimensions of the ion and electron demagnetized regions, the location of the separatrices, the exhaust flow, etc. (Burch et al., 2016c), which is a very difficult task.

The first basic assumption that makes possible the conversion from temporal to spatial data consists in assuming the *PSs* to be stationary in their proper frame, even if this frame, relatively to the *s/c*, can undergo variable accelerations in all directions, directly driven by the incident solar wind or due to local surface waves. The fact that the proper frame of the structure can experience accelerations can be exemplified, concerning the *MP*, by the existence of multiple and close crossings, such as those observed on 16 October 2015 (Rezeau et al., 2018), which are clearly due to a back and forth motion of the

*MP*. Under these conditions, it makes sense to draw a complex *s/c* path across a fixed structure, this relative motion being mainly due, in reality, to motions of the *MP* itself, rather than due to the *s/c* motion, which is quite slow. This assumption has long been used by experimenters for drawing hand-made sketches to interpret data in the reconnection context (see Figure (3) of Burch et al. (2016c), reproduced hereafter in the left part of Figure (8)).

The observed *PSs* are not always strictly stationary in their own frame. They can undergo modifications during the crossing due, for instance, to slowly growing MHD instabilities. We will show that these departures -even weak- from strict stationarity can lead to difficulties if the usual methods are used without caution for determining the relative motion between a structure and a *s/c*. For a quasi-1D structure for instance, the determination of the velocity components along the two quasi-invariant directions can be very inaccurate. This property, which is mentioned in the very recent review paper by Shi et al. (2019) will be demonstrated hereafter in this paper. We will show that any weak non-stationarity causes these components to diverge when using a method that assumes strict stationarity. The projection of the trajectory along the 1D direction is actually not much affected by this problem, but it is difficult to know *a priori* when the second and the third component can be reliably used or not. In the present paper we will therefore relax the assumption of strict *PSs* stationarity and replace it by a more moderate "quasi-stationarity" assumption. This means that we consider the *PS* to be stationary on time scales that are smaller than the time needed for the crossing of the entire *PS* (namely the *MP* crossing). In this sense we will discriminate the "global" from the "local" features of the *PS* characterizing, respectively, the entire *PS* and its sub parts. In the experimental example given below, the stationarity is assumed on  $\sim 10$  data points only ( $\sim 0.1$  s) while the global crossing takes  $\sim 1200$  points ( $\sim 10$  s). It therefore concerns a portion of about 0.8% of the total *MP* width. We will characterize as much as possible the local features of a *PS*, taking into account the possible slow modifications that can affect its structure during the crossing time. This will enable us to investigate its internal structure. Such information cannot be obtained by methods addressing the *PS* as a whole (e.g.: the MVA method Sonnerup and Cahill (1967) or the BV method Dorville, Belmont, Rezeau, Aunai, and Retinò (2014b) both returning a *global frame* known as LMN frame, where N is the direction of the normal and M and L are two other directions perpendicular to N and to each others). The methods that use multiple field and particle data sets may *a priori* be very beneficial for investigating *PSs*. But they can be difficult in practice because the different data sets often evidence gradients that are shifted from each other. This can be interpreted as the presence of different discontinuities. For instance, the *MP* is sometimes made of a slow shock (mainly seen on particles) and a rotational discontinuity (mainly seen on the magnetic field) (Dorville, Belmont, Rezeau, Grappin, & Retinò, 2014a).

Recently it has been possible to determine local *PS* normals thanks to methods providing a point-by-point reference frame (hereafter defined as a "*local frame*" in contrast to the "*global frame*" valid for the entire *PS*). These methods allow one to account for the spatio-temporal modifications of the orientation of the crossed *PS* (MDD (Denton et al., 2018; Shi et al., 2005) and LNA (Rezeau et al., 2018) techniques). When the local variations are quasi 1D in particular, these methods are efficient to obtain the corresponding varying normal (and the dimensionality, 1D or not, can be determined thanks to the MDD technique itself).

On the other hand, even if one can determine the dimensionality of the local variations as well as the local normal when it exists, the geometrical shape of the *PS* cannot be determined without strong hypotheses. When a *s/c* crosses a *PS*, the measurements provide data only along its trajectory. Beyond the determination of a local normal, one would like to determine the shape of the observed *PS* all around, in the vicinity of the trajectory. This problem is referred in the literature as a "reconstruction prob-



lem". The most known method consists in assuming the structure is stationary and that the relative path of the s/c with respect to the structure is just a straight line, traveled with a constant velocity. This knowledge is then used as a "boundary condition" for integrating the MHD Grad-Shafranov equations. This has been done under different assumptions: 2D or 3D structure, stationary or slowly evolving, with a computation based on MHD or electron-MHD equations (see for instance Sonnerup, Hasegawa, Teh, and Hau (2006), Hasegawa, Sonnerup, Eriksson, Nakamura, and Kawano (2015), among many other papers). It has also been applied to MMS observations of the electron diffusion region observed on 16 October 2015, 13:07 UT, nearly one minute later than the case we study Burch et al. (2016c); Hasegawa et al. (2017).

Our paper does not deal with such reconstructions, but with the determination of the path of the s/c relative to the PS. It can be understood as a necessary first step, prior to any reconstruction study. As this path can be, as it will be shown hereafter, quite different from a straight line traveled at a constant velocity, relaxing this assumption should allow to greatly improve the reliability of the reconstruction results. Obtaining the path information is the object of this paper. Beyond the straight line assumption, efforts have been made to improve the determination of the spacecraft path across the magnetopause, by considering different (but pre-determined) forms for this path Hasegawa et al. (2004); Q. Hu and Sonnerup (2003). Other authors have taken into account possible intrinsic temporal evolution of the structures Hasegawa, Sonnerup, Hu, and Nakamura (2014); Hasegawa, Sonnerup, and Nakamura (2010); Sonnerup and Hasegawa (2010). However, in all these studies the spacecraft velocity, even locally, is assumed to be the deHoffmann-Teller velocity, whereas the target of this paper is to recover the velocity without any *a priori* assumption.

(De Keyser, 2008) has introduced a different method that he called "empirical reconstruction". It is a multi-spacecraft method that allows determining a s/c path in the 1D hypothesis, and even in the 2D hypothesis, but under restrictive assumptions: no plasma flow across the *PS*, the 2D shape is supposed known *a priori* (for instance it is a surface wave).

Note that the integration of the flow normal velocity, used in (De Keyser, 2008) and also in BV (Dorville et al., 2014a) (which uses the magnetic field  $\mathbf{B}$  and the ion velocity  $\mathbf{V}$ ) to determine the path along the normal, is very sensitive to inaccuracies in the determination of the normal direction. The large tangential flows that exist in the magnetosheath can indeed, when projected on an approximate normal direction, provide an apparent normal flow that is very inaccurate, even if the inaccuracy in the normal direction is small.

Finally, the Spatio-Temporal Difference technique (STD, (Shi et al., 2006)) deserves a separate discussion since, in contrast to the other methods, it is not affected by any of the strong assumptions previously discussed, except for the stationarity of the *PS*. With respect to a fixed frame, the STD method is able to recover the *PS* velocity ( $\partial_{t,0}\mathbf{X}$ , where  $\mathbf{X}$  is the *PS* position) by means of inversion of the equation

$$\partial_{t,sc}\mathbf{B} = \partial_{t,0}\mathbf{X} \cdot \nabla\mathbf{B} \quad (1)$$

The left hand side (LHS) term represents the temporal derivative of the magnetic field in the *s/c* frame and the right hand side (RHS) term involves the spatial derivative. These are computed by means of the reciprocal vector method (Chanteur, 1998) that exploits the multi-point measurement of missions such as CLUSTER or MMS (Burch et al., 2016c)). For the sake of clarity, we have specified here and everywhere afterwards in the text that the methods are applied to the magnetic field data. These methods remain valid, however, if  $\mathbf{B}$  is replaced by any other quantity (e.g.:  $\mathbf{E}$ ,  $\mathbf{V}_i$ ,  $\mathbf{V}_e$ , etc...). The assumption of stationarity causes the method to fail when the term  $\partial_{t,0}\mathbf{X} \cdot \nabla\mathbf{B}$  becomes comparable to or smaller than the intrinsic temporal variations of the *PS* magnetic struc-

ture:  $(\partial_{t,0}\mathbf{B})$ , *i.e.* when the *PS* can no longer be considered as strictly stationary in its own reference frame. When the intrinsic temporal variation of the *PS* is not negligible, we will have to replace Equation (1) by Equation (2), which is its generalization:

$$\partial_{t,sc}\mathbf{B} = \partial_{t,0}\mathbf{X} \cdot \bar{\nabla}\mathbf{B} + \partial_{t,0}\mathbf{B} \quad (2)$$

The subscripts 0 indicate the particular frame used: supposing that a quasi-stationary frame does exist, in which the intrinsic variation  $\partial_{t,0}\mathbf{B}$  is minimum, the term  $\partial_{t,0}\mathbf{X}$  represents the *s/c* velocity in this frame.

This paper will present new methods to perform this generalization (sections 2.1.2 and 2.1.3). These new methods are tested on artificial magnetic fields mimicking linear (section 3.1.1) and back and forth motions (section 3.1.2) of the *MP*. The results are compared to those from a modified version of the STD method able to suppress singularities occurring to STD in analyzing nearly 1D *PSs* (section 2.1.1). We will present 1D and 2D reconstructions of the MMS *s/c* path during two real *MP* crossings (section 3.2). Finally, a summary of our results and a discussion of future prospects for these methods is presented in section 4.

## 2 Methods

In the following sections, we explain the methods used to compute the *s/c* path with respect to the observed *PS*. In sub-section (2.1) we discuss the problems that occur when using the STD method for that purpose and how we solve them. This is done in two different ways: via the suppression of the singularities that occur in STD when the *PS* is not sufficiently three-dimensional (sub-section 2.1.1) and via new methods that extend the computation beyond the strict stationarity assumption (sub-sections 2.1.2 and 2.1.3). In sub-section (2.2) we show how to integrate the *s/c* velocity to obtain the *s/c* path. Finally, in sub-section (2.3), we present the optimization procedure we adopt to determine the optimal values for the different threshold parameters that are used in the methods.

### 2.1 The computation of $\partial_{t,0}\mathbf{X}$

#### 2.1.1 From STD to $STD^+$ : the suppression of singularities

As previously discussed, the STD method of (Shi et al., 2006) computes point-by-point values of  $\partial_{t,0}\mathbf{X}$  by inverting Equation (1):

$$\partial_{t,0}\mathbf{X} = \partial_{t,sc}\mathbf{B} \cdot [\bar{\nabla}\mathbf{B}]^{-1} = \frac{\partial_{t,sc}\mathbf{B} \cdot [\bar{\nabla}\mathbf{B}]^A}{\det[\bar{\nabla}\mathbf{B}]} \quad (3)$$

In this expression, the superscript *A* indicates the adjoint matrix. Combined with the MDD method (Shi et al., 2005), the STD allows computation of both the dimensionality (1D, 2D or 3D) of the space variations and the orientation of the *PS*. It also allows one to calculate the thickness of the crossed *PS* (via the cumulative sum of  $\partial_{t,0}\mathbf{X}$ ) under the strong assumption that  $\partial_{t,0}\mathbf{B} \ll \partial_{t,sc}\mathbf{B}$  and  $\partial_{t,0}\mathbf{B} \ll \partial_{t,0}\mathbf{X} \cdot \bar{\nabla}\mathbf{B}$ . As we observe from Equation (3), the method is particularly sensitive to the conditions for which the determinant  $\det[\bar{\nabla}\mathbf{B}]$  becomes very small. This determinant tends to zero everywhere the variations are not sufficiently three-dimensional, *i.e.* everywhere there is locally one or two nearly invariant directions. Under these conditions, the numerator and denominator of Equation (3) both tend toward zero and the result becomes undetermined: its value then strongly depends on any noise or to any departure from a strict stationarity that can make the numerator null at a place slightly different from the denominator.

Following (Shi et al., 2006), this problem can be in practice circumvented by reducing the matrix  $\bar{\nabla}\mathbf{B}$  used in Equation (3) to its non singular part, *i.e.* by retaining only the largest partial derivatives, the number of which depends on the dimensionality of the *PS*. For instance, when the variations are approximately 1D (with a threshold empirically determined for the eigenvalues), one can keep only the derivative along the local normal and determine only this normal trajectory, so giving up for the determination of a 2D or 3D path. However, one may foresee that this reduction process would cause an unnecessary loss of information. Actually, the 2D or 3D local variations that always exist may be significant enough, even if weak, to be used for determining the 2D or 3D paths. (Shi et al., 2006) also evoked the possibility of adding some artificial noise (called "random errors") to ensure that, even in the strictly 1D case, the determinant is non-null almost everywhere. This artificial noise actually would come in addition to the "natural noise" as defined in the present paper (see section 3.1). The velocity component along the maximum gradient direction would *a priori* not be much affected by this noise addition. On the contrary, the two other components, which would only be due to the noise when the physics is really 1D, should then be rejected, even out of the singular points. This method would therefore not allow one to reach the goal proposed in the present paper, which is to draw as much information as possible from the small variations that can be extracted out of the noise.

For the sake of clarity, let's define the directions  $\mathbf{l}$ ,  $\mathbf{m}$  and  $\mathbf{n}$  as the three linearly independent directions of the local frame coincident to the eigenvectors of  $\mathbf{G} = \bar{\nabla}\mathbf{B} \cdot \bar{\nabla}\mathbf{B}^T$  associated, respectively, to the minimum, intermediate and maximum eigenvalues of  $\mathbf{G}$ . Note that the two frames,  $\mathbf{lmn}$  and  $\mathbf{LMN}$  (the latter coming from MVA, its axes corresponding respectively to the largest, intermediate and minimum variance directions) have the same "normal" directions ( $\mathbf{n} = \mathbf{N}$ ) as soon as the local properties are identical to the global ones, but that their axes in the tangential plane are not the same. The eigenvectors associated with the smallest eigenvalues of  $\mathbf{G}$  are often significantly affected by high frequency variations, which may lead one to prefer, for some applications, projecting the motion onto a more stable global frame. In Figure (1), the time interval chosen in this paper for discussing the methods is presented. It shows the high frequency irregular oscillations of the GSE components of the  $\mathbf{m}$  and the  $\mathbf{l}$  directions (panels 1.c and 1.d) in contrast to the more stable  $\mathbf{n}$  direction (panel 1.b) during the 16 October 2015, 13:05:30+60s UT (*i.e.*, 13:05:30–13:06:30 UT) *MP* crossing (the magnetic field is shown in panel 1.a).

The method that we propose consists in taking into account as much as possible any small departure from the 1D geometry in order to determine 2D or 3D paths across the magnetic structure. When the structure is approximately mono-dimensional, the local determinant has a very small value, fluctuating in time and changing its sign. It is the product of one large eigenvalue, with little inaccuracy, and two small eigenvalues with possibly fluctuating signs. Each of the zero crossings of the small eigenvalues leads to a singularity for the velocity component in the direction of the corresponding eigenvector. This effect is evidenced in Fig. (2), as well as the effect of the corrections made.

In this figure, the results are shown in GSE frame, so that all components are to be corrected in the same way. It is clear that in the local ( $\mathbf{l}$ ,  $\mathbf{m}$ ,  $\mathbf{n}$ ) frame, only the components  $\mathbf{l}$  and  $\mathbf{m}$  can be concerned by the singularity problem since the eigenvalue corresponding to the largest spatial derivative is never zero as long as the signal is not strictly constant. Nevertheless, this local frame is varying inside the magnetopause crossing, so that even the global  $\mathbf{N}$  direction (as obtained via a global MVA or by average on the local  $\mathbf{n}$  directions) is not exempted from the singularity problem: even a 1 degree variation in the direction of  $\mathbf{n}$  has significant consequences in the global normal direction if the singularity leads to values larger than 100 times the neighbouring values. This is important since we need to know the velocity in a fixed frame to be able to calculate the path by integration.

As we do not know *a priori* at which threshold the structure is to be considered as 1D or not, we propose here to consider by default that it is 3D and derive the three components of the velocity. We do not add any artificial noise and we expect that the "natural one" will not change much the results as soon as we get rid of the singularities in the calculated velocity, which would lead to non physical jumps in the calculated path. Doing so, the choice of keeping the 1D, 2D or 3D projections of the path can be done *a posteriori*.

In order to avoid the reduction process (determining only one projection of the path), we use here the entire  $\bar{\nabla}\mathbf{B}$  matrix with a procedure for suppressing automatically the singularities affecting some components of the velocity of the structure when using the original STD method without caution. For this purpose, we introduce a "very local" correction to force the numerator of Equation (3) to be zero at the times  $t^*$  when the denominator ( $\det[\bar{\nabla}\mathbf{B}]$ ) is zero. In order to do so, we add to each of the three components of  $\partial_{t,sc}\mathbf{B} \cdot [\bar{\nabla}\mathbf{B}]^A$  a signal made by a linear combination of gaussian curves each of which 1) is centered at times  $t^*$ , 2) has a amplitude equal to  $-\partial_{t,sc}\mathbf{B}(t^*) \cdot [\bar{\nabla}\mathbf{B}(t^*)]^A$  and 3) is narrow enough not to modify the signal for a period larger than 1% of the global period analyzed (*i.e.*  $\simeq 10$  data points for the cases studied in this paper) and not to overlap the nearby corrections. In section 3.2.1 the LHS of Equation (3) with and without corrections will be compared for a real case study.

Hereafter, we dub the above method STD<sup>+</sup>. It aims at circumventing pragmatically the problem of singularities but without tackling directly the main cause of the problem: the small non-stationarities affecting the data. As previously mentioned, the STD method assumes strict stationarity. Unfortunately, the presence of weak non stationarities can cause infinite values for some components of the velocity determined by this method. Even if the non-stationarity  $\partial_{t,0}\mathbf{B}$  is weak, it cannot be ignored wherever it is non-negligible with respect to the convective term  $\partial_{t,0}\mathbf{X} \cdot \bar{\nabla}\mathbf{B}$ . This systematically occurs when the latter tends to zero, *i.e.* wherever the  $s/c$  is approximately at rest with respect to the *PS*. In this case,  $\partial_{t,sc}\mathbf{B}$  must be replaced by  $\partial_{t,sc}\mathbf{B} - \partial_{t,0}\mathbf{B}$  in the numerator of Equation 3. It is then clear from this equation that the effect of this change on the determination of  $\mathbf{X}$  is all the larger as the determinant of  $\det[\bar{\nabla}\mathbf{B}]$  is smaller, *i.e.* when the spatial variations are not sufficiently three-dimensional (we know that  $\det[\bar{\nabla}\mathbf{B}] \rightarrow 0$  whenever one or two eigenvalues tend to zero). Note that, at the limit  $\det[\bar{\nabla}\mathbf{B}] = 0$ , the STD method leads to divergences whatever the velocity  $\partial_{t,0}\mathbf{X}$  is. Therefore, in order to generalize the computation of the  $s/c$  velocity ( $\partial_{t,0}\mathbf{X}$ ) to non stationary *PS* cases, we need to distinguish the sources of the time variations  $\partial_{t,sc}\mathbf{B}$  of the magnetic field seen by the  $s/c$ : convective ( $\partial_{t,0}\mathbf{X} \cdot \bar{\nabla}\mathbf{B}$ ) and pure temporal variation of the *PS* itself ( $\partial_{t,0}\mathbf{B}$ ). We will therefore have to retrieve the  $\partial_{t,0}\mathbf{X}$  term from Equation (2) instead of Equation (1), *i.e.* without neglecting the intrinsic variation  $\partial_{t,0}\mathbf{B}$ .

In the following two sub-sections, we explain how we manage to obtain  $\partial_{t,0}\mathbf{X}$  from Equation (2).

### 2.1.2 The Multi-Variate fit method (MVF)

In Equation (2), the unknowns are the  $\partial_{t,0}\mathbf{X}$  and the  $\partial_{t,0}\mathbf{B}$  terms while the  $\partial_{t,sc}\mathbf{B}$  and the  $\bar{\nabla}\mathbf{B}$  terms are computed from data via a temporal derivative and the reciprocal vector method (Chanteur, 1998) thanks to the multi-point measurements provided by MMS. In any but the local *lmn* frame, this equation represents an intertwined relation between the temporal and spatial variations of the different components of  $\mathbf{B}$  via the  $\mathbf{X} \cdot \bar{\nabla}\mathbf{B}$  term. The determination of  $\partial_{t,0}\mathbf{X}$  and  $\partial_{t,0}\mathbf{B}$  can be done by means of a multi-variate fit procedure assuming the two unknowns are approximately constant over a short interval lasting  $p$  experimental points. A fit is performed that minimizes analytically the total squared difference between the observed temporal variations ( $\partial_{t,sc}\mathbf{B}$ ) and the reconstructed ones ( $\partial_{t,0}\mathbf{X} \cdot \bar{\nabla}\mathbf{B} + \partial_{t,0}\mathbf{B}$ ), normalized to the mean magnetic field tempo-

ral derivative:

$$D \equiv \frac{\sum_p \left\{ \sum_i [\partial_{t,sc} B_i - (\partial_{t,0} X_j \partial_j B_i + \partial_{t,0} B_i)]^2 \right\}_p}{\sum_p \left[ \sum_i (\partial_{t,sc} B_i)^2 \right]_p} \quad (4)$$

where  $i, j = \{x, y, z\}$ . Once the  $\partial_{t,0}\mathbf{X}$  and the  $\partial_{t,0}\mathbf{B}$  terms are obtained, a selection procedure is made according to the comparison between the associated error (given by the Equation (4)) and a threshold  $D_{lim,MVF}$ : if  $D > D_{lim,MVF}$  the results are discarded, otherwise the results are retained. Since  $D$  is expected to be very small for a fit result to be retained,  $D_{lim,MVF}$  is chosen to be very small too, e.g.:  $10^{-1}$  or  $10^{-2}$ . The fits are performed on a number of data points that can vary (in accordance with the optimization procedure described in appendix A.1) from a lower integer value  $p_{min}$  to a maximum integer value  $p_{max}$  based on the local curvature of the curve to be fitted. We use MMS magnetic field data recorded in "burst mode" at  $\nu_s = 128\text{Hz}$  (Torbert et al., 2016) and preliminarily filter data in Fourier space to frequencies below  $\nu_c$  in order to select the frequency windows to observe. This filtering is necessary to get rid of the small scale fluctuations and waves that are present at the MP and that have an intensity much higher than the instrument noise (Rezeau, Roux, & Russell, 1993). Then we set

$$\{p_{min}, p_{max}\} = \{\text{int}\left(\frac{\nu_s}{4\nu_c}\right), 13\}. \quad (5)$$

As a matter of facts, the highest frequency component of a signal filtered using  $\nu_c$  could still have large variations in a period  $\nu_c^{-1}/4$  long. This period corresponds to  $\nu_s/(4\nu_c)$  data points if the original signal is probed at  $\nu_s$ . On the other hand, we do not want a fit to represent more than one hundredth of the total crossing duration. Since the  $MP$  crossing examined in this study are no longer than 10s and thanks to the high magnetic field probing rate of MMS, the maximum time period corresponds to 13 data points. The  $\partial_{t,0}\mathbf{X}$  and the  $\partial_{t,0}\mathbf{B}$  terms which do not survive the selection procedure are replaced by means of interpolation. This method assumes the  $PS$ s to be stationary for, at least, an interval  $p\nu_s^{-1}$  long, *i.e.* much smaller than the periods during which other methods assume the  $PS$ s to be stationary.

### 2.1.3 The Single-Variate fit method (SVF)

The working principle for MVF is the minimization of the total error  $D$  which is the squared modulus of the vectorial normalized error when fitting the temporal derivative of  $\mathbf{B}$  (Equation (4)). For this reason, the MVF method is not able to discriminate which component of Equation (2) causes the fit to be rejected: a large error in the  $l$  component leads to rejection of the entire velocity while the  $n$  component might well be determined. The method can be improved by performing the fit procedure in the local  $lmn$  frame. In this frame, the  $\bar{\nabla}\mathbf{B}$  matrix is diagonal so that the three components of Equation (2) do not share common unknowns; therefore the fit procedure can be performed independently for each component, disentangling the high quality fits of one component from the low quality fits of the others. Nevertheless, it is worth remembering that in some cases the  $lmn$  frame is far from being stable (remember Figure (1)): the SVF method can be applied anyway in these cases but it is clear that the local  $lmn$  frame has then no real physical significance. Only the directions corresponding to large derivatives are expected to be reliable and thus stable.

## 2.2 The projection and the integration of $\partial_{t,0}\mathbf{X}$

STD<sup>+</sup>, MVF and (in some cases) SVF, generally compute a 3D  $\partial_{t,0}\mathbf{X}$ ; the goal of this section is to explain how we obtain a 3D path  $\mathbf{X}(t)$  from  $\partial_{t,0}\mathbf{X}$ . Actually, due to an intrinsic limitation of the methods which base their computations on the  $\bar{\nabla}\mathbf{B}$  matrix, we will first focus on the projection of  $\partial_{t,0}\mathbf{X}$  on the eigenvector that corresponds to the largest eigenvalue (here called  $\mathbf{n}$ ), which is *a priori* the best determined component. The

final result will be therefore a 1D displacement  $X_N(t)$  describing the position of the  $s/c$  with respect to the  $PS$  along its normal as a function of time. The reason why the  $\mathbf{m}$  and  $\mathbf{l}$  components of  $\partial_{t,0}\mathbf{X}$  may be less accurate than the  $\mathbf{n}$  component can be easily understood. Writing Equation (1) in the  $\mathbf{lmn}$  frame, which corresponds to the eigenvectors of  $G \equiv \nabla\mathbf{B} \cdot \nabla\mathbf{B}^T$ ,  $\partial_{t,0}X_i \propto 1/\lambda_i$  (with  $i = \{l, m, n\}$ ), which clearly goes to infinity when  $\lambda_i$  goes to zero. We come here across the same difficulty that was causing the singularities in STD. In the rest of this section, we will concentrate only on the best determined normal projection of the  $s/c$  path. We will however show in section 3.2 that 2D maps of the  $s/c$  path can be obtained quite satisfactorily under favorable conditions ( $\lambda_m$  not much smaller than  $\lambda_n$  during the major part of the crossing).

Due to the previous considerations and since we ultimately need a global direction along which to plot the  $s/c$  path, the 1D map  $X_N(t)$  is computed in the following way:

$$X_N = \int (\partial_{t,0}\mathbf{X}(t) \cdot \mathbf{n}(t)) (\mathbf{n}(t) \cdot \mathbf{N}_{glob}) dt \quad (6)$$

where  $\mathbf{N}_{glob}$  is defined as the mean of the  $\mathbf{n}(t)$  directions computed over the main magnetic field gradient interval (between the two vertical dotted red lines in Figure (1)). This double projection ensures that we use the best determined  $\mathbf{n}$  component of the  $\partial_{t,0}\mathbf{X}$  velocity, but projected on the global direction  $\mathbf{N}_{glob}$ . The projection involved in Equation (6) is performed only when the  $PS$  is quasi 1D and the magnetic field variations are related to the main current layer. Following (Rezeau et al., 2018), these requirements can be checked for each data point by using the parameters  $K_{1D}$  and  $K_{dB}$ . We require that

$$(\lambda_n - \lambda_m)/\lambda_n > K_{1D} \quad (7)$$

with  $K_{1D} \ll 1$  and

$$dB/dt > K_{dB} [dB/dt]_{max} \quad (8)$$

with  $K_{dB} \ll 1$ ,  $B \equiv |\mathbf{B}|$  and, as usual,  $\lambda_n$  and  $\lambda_m$  are the two largest eigenvalues of  $G$ .

The time derivatives  $dB/dt$  are those measured in the  $s/c$  frame. As before (section 2.1.2), the data points that do not survive the selection procedure are replaced by means of interpolation.

### 2.3 A Gradient-Directed Monte Carlo approach for thresholds decision

The methods described in the previous sections require values for a large number of thresholds. These thresholds are the minimum and the maximum number of fit points for the MVF and the SVF methods ( $p_{min,SVF}$ ,  $p_{min,MVF}$  and  $p_{max,SVF}$ ,  $p_{max,MVF}$ ), the thresholds that set a limit to the fit errors for a SVF or a MVF result to be retained or not ( $D_{lim,SVF}$  and  $D_{lim,MVF}$ ), and the thresholds for the selection procedures of 1D  $PS$ s associated with large currents ( $K_{1D}$  and  $K_{dB}$ ). In the present study we fix manually the parameters  $p_{min,SVF}$ ,  $p_{min,MVF}$ ,  $p_{max,SVF}$  and  $p_{max,MVF}$  as discussed in section 2.1.2 in order to limit the fit procedures to periods between 0.04 and 0.1s; this allows to handle a sufficient number of data points per fit and fits per event. We collect all the remaining parameters in a vector

$$C_r \equiv \{D_{lim,SVF}, D_{lim,MVF}, K_{1D}, K_{dB}\} \quad (9)$$

that points to a general state in a 4D phase space  $\mathcal{F}_{C_r}$ . The spacecraft displacement  $X_N(t)$  is an unknown nonlinear function of the  $C_r$  components. As it is very sensitive to small variations of  $C_r \in \mathcal{F}_{C_r}$ , it is reasonable to let it automatically evolve toward values that



make the SVF and MVF outcomes to be as close as possible to each other wherever they can both be determined and make this common interval of validity as long as possible. Such a problem is efficiently solvable by means of an iterative minimization procedure based on a gradient descent algorithm known as Gradient-Directed Monte Carlo Approach (GDMC, (X. Hu, Beratan, & Yang, 2008)). The GDMC technique is a stochastic approach for optimization procedures. It was conceived to find the best  $C_r^*$  that optimizes some result  $R(C_r)$  via the random sampling of the best candidates for  $C_r^*$  in regions of  $\mathcal{F}_{C_r}$  as suggested by  $-\nabla F$ , where  $F$  is a function that evaluates the distance between  $R(C_r)$  and the expected result. In our case, we use the GDMC to select the optimal  $C_r^*$  that minimizes (maximizes) the distance (the shared period) between the two  $X_N(t)$  resulting from the application of the SVF and MVF methods to the same data set. The GDMC approach has been conceived in molecular design to study the proteins folding properties (X. Hu et al., 2008) and, since it is necessary to obtain the optimal solution in our problem, we describe in detail how we adapt it for our purposes in Appendix (A.2).

### 3 Results

In the following sections we apply the methods that we have described to artificial and real magnetic fields representing -and probed across- the Earth's Magnetopause (*MP*). During southward IMF conditions, the *MP* is characterized by a jump in magnetic field from positive values (within the magnetosphere) to negative values (within the magnetosheath). With this magnetic configuration we use the magnetic field in Equations (3) and (2) to recover, for each case, three different *s/c* displacements  $X_N(t)$  across the *MP* and, therefore, the magnetic field profile across this physical discontinuity. The *MP* has gradients also in other quantities ( $\mathbf{E}$ ,  $\mathbf{V}_i$ ,  $\mathbf{V}_e$ , etc...). The profiles of these quantities can be investigated in the same way, but we will not do this in the present paper.

#### 3.1 Tests on artificial magnetic fields

The artificial magnetic fields we use to test the routines are created by a linear combination of a 1D model ( $\mathbf{B}_{\text{model}}$ ) and a random noise ( $\mathbf{B}_{\text{random}}$ ). The  $\mathbf{B}_{\text{model}}$  term is

$$\mathbf{B}_{\text{model}}(x) = \{0, B_{y0} + B_{y1}\tanh(\frac{x}{L}), B_{z0} + B_{z1}\tanh(\frac{x}{L})\} \quad (10)$$

so that the *MP* normal is oriented toward the X direction and has a thickness equal to  $\sim 6L$ , if one define the thickness as twice the distance where each component of the current ( $\partial_x(\mathbf{B}_{\text{model}})$ ) falls to 1% of its maximum value, *i.e.* twice the distance  $x^*$  where:

$$L\partial_x(\tanh(x^*/L)) \simeq k^* \quad (11)$$

with  $k^* = 0.01$ . Each virtual *s/c* measures a slightly different  $\mathbf{B}_{\text{model}}$  since their trajectories are modeled to be  $\sim 10$  km apart, similar to the smallest MMS separation.

Finally, the "noise" is designed to model all the waves and turbulence always present in these regions, and which have typically amplitudes much larger than the instrumental errors Rezeau et al. (1993). This noise, superposed to the large scale fields could have an impact and may therefore alter the results. Such a "natural noise" is observed on the small scale fluctuations that remain after the filtering procedure discussed in section (2.1.2). Its amplitude and spectrum have been chosen differently for the test signals in the two following examples. In both cases, the amplitudes remain compatible with the observations and the spectrum decays at frequencies above  $\nu_c$ , the upper frequency limit above which the MMS data are filtered. The second example contains more large scale variations, mimicking the possible large scale evolution of the magnetopause *PS*.

##### 3.1.1 A straight crossing

Figure (3) shows results for the first test case in which the virtual spacecraft cross an artificial *MP* along a straight path traveled at constant velocity. The modeled mag-

netic field  $\mathbf{B}_{\text{model}}$  is defined by Equation (10) with  $\{B_{y0}, B_{y1}, B_{z0}, B_{z1}\} = \{12, 0, 10, 30\}$  nT and  $L = 250$  km. The mean MDD normal found from the virtual s/c data along their paths is  $\mathbf{N}_{MDD} \simeq \{0.99, -0.02, 0.02\}$ , which is slightly different from the true normal  $\{1, 0, 0\}$  due to the noise  $\mathbf{B}_{\text{random}}$ . The displacements  $X_N$  found from the three methods are plotted in panel 3.c in comparison with the model (the result obtained with STD is the same as the one obtained with  $\text{STD}^+$  and therefore is not shown). Also plotted in panel 3.a and 3.b are the magnetic fields and the currents found from the curlometer technique; the panel 3.d shows the differences between each pair of  $X_N$  (call it  $\Delta X_{N,ij}$  with  $i, j$  equal to a 2-permutation choice between  $\text{STD}^+$ , SVF and MVF). From panel 3.d we observe that

1. During the time for which the current is large, the  $\Delta X_{N,ij}$  are comparable to - and often lower than- 10 km, marked by the horizontal black dashed line. This is roughly equal to the mean electron inertial length  $\delta_e$  and the MMS inter-spacecraft distance adopted by the mission to probe the *MP* at the magnetospheric nose (Burch & Torbert, 2016a);
2. The width of the main current layer defines the limits of the *MP* so that the total *MP* thickness can be estimated by the difference of the two displacements  $X_N$  at the upper and lower limits of this interval. In this case, these limits are at about  $t \sim 6$ s and  $t \sim 15$ s so that the *MP* thickness is  $\sim 1.4 \times 10^3$  km thick, *i.e.*  $\sim$  six times the parameter  $L$  used in Equation (10) for this case, as expected;
3. Outside the  $[6, 15]$ s interval, the differences  $\Delta X_{N,ij}$  become larger at the left and the right sides. In these regions the results should be ignored since the displacements are no longer associated with the main *MP* current.

From these  $X_N$  values we can determine the relative error of the s/c location within the  $[6, 15]$ s interval, which, for this case, can be estimated to  $\sim \Delta X_{N,ij}/(6L) \simeq 7 \cdot 10^{-3}$ .

### 3.1.2 A back and forth crossing

Figure (4) shows a test case that is more similar to observations than the test performed in the previous section, both in regards to the *MP* thickness and the kinematics. The artificial *MP* is defined using Equation (10) with  $\{B_{y0}, B_{y1}, B_{z0}, B_{z1}\} = \{5, -15, 10, 30\}$  nT and  $L=70$  km. The *MP* is now  $6d_{i,MSH}$  wide (where  $d_{i,MSH}$  is the ion inertial length measured within the magnetosheath). There is now a back and forth motion starting at about the middle of the crossing with two stagnation points at  $t_1 = 3.75$ s and at  $t_2 = 4.3$ s.

Moreover, we take  $\mathbf{B}_{\text{random}}$  with a larger amplitude (by a factor of 3.5). The electric current is so made clearly "noisier" than that computed in section 3.1.1 (compare panel 3.b of Figure 3 with panel 4.b of Figure 4) and so closer to the observed one (panel 6.b, Figure 6). Let us recall that what we call "noise" in this paper is not the instrumental one, which is quite negligible, but the "plasma noise", just discussed above. Note that this "plasma noise" can also model any other non stationarity affecting the boundary, such as the large scale ones that affect the magnetopause in the vicinity of a reconnection X point.

Looking at panels 4.c and 4.d we observe that the  $\text{STD}^+$ , the MVF and the SVF methods yields quite similar displacements (as before, the STD results are not shown being equal to the  $\text{STD}^+$  results); SVF gives the best results, which is closest to that of the model. The agreement between MVF and  $\text{STD}^+$  is expected since no pure temporal variations are introduced in  $\mathbf{B}_{\text{model}}$ . The enhancement of the noise makes the range of applicability of the three routines smaller than  $6L$  and prevents them to be safely applied outside the  $[2-5.5]$ s interval. For this reason our methods could not determine the total *MP* thickness which was about  $6L = 420$  km, about 1.5 times larger than what the methods detected. It is clear that this under-estimation is just due to the definition



of the *MP* thickness that has been used here and can easily be corrected. The *MP* thickness is defined as twice the distance  $x^*$  at which the asymptotic current falls to a fraction  $k^*$  of its maximum. Taking  $k^* = 0.01$  in Equation 11 is clearly too small with respect to the value of the noise. Using  $k^* = 0.1$  instead of  $k^* = 0.01$  would make the expected *MP* thickness ( $3.6L = 252$  km) equal to what is found. This must be kept in mind for future studies.

## 3.2 Applications to MMS data

### 3.2.1 Case study I: 1D and 2D projections of the MMS path

#### The 1D projection

We applied the STD<sup>+</sup>, SVF and MVF methods to magnetic field data probed in burst mode (128 Hz) by MMS on 16 October 2015 during the 13:05:30+60s UT crossing. This crossing is very well known in the literature (Burch et al., 2016c; Le Contel et al., 2016; Rezeau et al., 2018; Torbert et al., 2016) and so it is a good test case to benchmark our methods. During this crossing, there was a reconnection outflow jet within the *MP* coming from a nearby northward magnetic reconnection event that was probed by MMS just a minute later (Figure 3 of (Burch et al., 2016c)); the reconnection outflow velocity, reaching a maximum of  $\sim 350$  km/s near the magnetosheath side, prevents determination of the normal displacement  $X_N(t)$  from integration of the normal component of the bulk velocity, even though the outflow is mostly tangential to the *MP*. This is because even a small inaccuracy (say  $\pm 5^\circ$ ) in the determination of the normal direction can cause the integration to yield an erroneously large normal flow.

The crossing occurred at  $[8.3, 8.5, -0.7]R_E$  in the GSE frame, when the IMF was southward so that there was a clear rotation of the magnetic field within the *MP*. This can be seen in Figure 5, where we plot the magnetic field hodogram. In this figure, the out-of-plane direction coincides with the mean MDD normal  $\mathbf{N}_{glob}$ , which is computed as the mean of the instantaneous MDD normals  $\mathbf{n}$  satisfying our dimensionality and variation conditions (Equations. 7 and 8) with the parameters  $K_{1D} = 0.73$ ,  $K_{dB} = 0.11$  within the [13:05:43 - 13:05:49] interval. The  $\mathbf{t}_2$  direction is the direction along which the tangential magnetic field varies the least.

In this reference frame, the resulting magnetic field is shown in panel 6.a of Figure (6): the  $B_n$  and the  $B_{t2}$  components are quasi-constant whereas the  $B_{t1}$  component has an irregular tanh dependence, changing from magnetospheric values ( $\sim 30$  nT at early times) to magnetosheath values ( $\sim -25$  nT at late times). The local peak in  $B_{t1}$  at around  $t = 15.0$ s has already been suspected to be caused by a back and forth motion of the *MP* (Rezeau et al., 2018). The panel 6.b shows the curlometer current; as expected the largest component is that directed toward the  $-\bar{t}_2$  direction. The modulus of the current reduces on the left and on the right extremes of the interval signing the overall *MP* thickness. The panel 6.c shows the  $X_N(t)$  resulting from five different methods. The STD<sup>+</sup>, SVF and MVF displacements are quite close to each other (see panel 6.d to evaluate their mutual distances  $\Delta X_{N,i,j}$ ), all confirming the back and forth motion, while the red and purple lines, which come from two different integrations of the ion velocity, are significantly different. The red curve results from the integration of the ion bulk velocity  $\mathbf{V}_i$  projected on  $\mathbf{N}_{glob}$ , i.e.  $\int \mathbf{V}_i \cdot \mathbf{N}_{glob} dt$ . The purple curve also results from the integration of  $\mathbf{V}_i$  but projected as shown in Equation (6), i.e.  $\int (\mathbf{V}_i \cdot \mathbf{n}(t)) (\mathbf{n}(t) \cdot \mathbf{N}_{glob}) dt$ . The red curve does not agree with those resulting from the other methods: it does not yield either the same *MP* thickness or the back-and-forth motion of the *MP*. The purple curve succeeds in finding the back-and-forth motion but fails to yield a thickness similar to those computed with the STD<sup>+</sup>, SVF and MVF methods. Since a non negligible  $B_n$  component is present, the *MP* is not a tangential layer and the differences between the purple curve and the STD<sup>+</sup>, SVF and MVF displacements are caused by the existence of a normal flow across the *MP*. The panel 6.e of Figure (6) shows the nor-

mal flow computed as  $[(\mathbf{V}_i - \partial_{t,0}\mathbf{X}) \cdot \mathbf{n}(t)](\mathbf{n}(t) \cdot \mathbf{N}_{glob})$  and normalized point-by-point to the normal component of the local Alfvén speed  $V_{a,n}$ . Comparing Figure (6) with Figure (5), where the color code indicates the magnitude of the normal flow, we observe that the normal flow tends to reach  $\pm V_{a,n}$  values everywhere the *MP* sub-structures tend to be purely rotational, which a quite satisfying result.

Let us now compare the spacecraft velocities obtained using Equation (3) when the singularities explicated in section 2.1.1 are corrected ( $\text{STD}^+$ ) and when they are not corrected (STD). Panel 6.f shows the modulus of the LHS terms of Equation (3), *i.e.*  $|\partial_{t,0}(\mathbf{X}_{STD})|$  and  $|\partial_{t,0}(\mathbf{X}_{STD^+})|$ . The orange curve is obtained by using Equation (3) without correcting the singularities. We observe that it is affected by large and very narrow spikes, that would lead to nonphysical jumps in the calculation of the s/c path. The figure shows also that the gaussian corrections do not modify the overall behaviour except during the very small periods where the STD results become large, preserving in this way the information provided by the original STD. They so allow computing the s/c path across the magnetopause.

Finally this crossing does not show any significant non-stationary behavior since the displacements from the SVF and MVF methods agree within a few percent with that of the  $\text{STD}^+$  method. This indicates that the  $\partial_{t,0}\mathbf{B}$  term in Equation (2), used by SVF and MVF, does not lead to a significant correction to the displacements. The conclusion is verified through a direct comparison of the three terms of each component of Equation (2). Figure (7) shows such a comparison. Panels 7.b, 7.c and 7.d compare the three terms of Equation (2) for each of its components and show that the  $\partial_{t,0}\mathbf{B}$  terms (green curves), though non negligible, are always smaller than the observed  $\partial_{t,sc}\mathbf{B}$  terms (blue curves) and the computed  $\partial_{t,0}\mathbf{X} \cdot \nabla \mathbf{B}$  terms (orange curves). This can explain why, at some times, the SVF and MVF results are closer to each other in panel d than that of  $\text{STD}^+$ , (see for instance between  $t = 15s$  and  $t = 18s$ ).

### The 2D projection

During the crossing the MDD eigenvalues ratios  $\lambda_m/\lambda_n$  and  $\lambda_l/\lambda_n$  (with  $\lambda_n > \lambda_m > \lambda_l$ ) oscillate around,  $1.2 \cdot 10^{-1}$  and  $9.5 \cdot 10^{-3}$ , respectively. The first and the second ratios are larger than  $10^{-1}$  and  $10^{-2}$  for, respectively, 37% and 19.5% of the selected time interval. Corrections due to the calibration errors (Denton et al., 2010) have been taken into account but results does not change significantly. These considerations suggest that, at least, a 2D reconstruction of the s/c path can be meaningful, since  $\lambda_m$  is not too much smaller than the  $\lambda_n$  for a relative long period of time.

Figure (8) shows the automatic calculation (AC) of the MMS path resulting from the application of the MVF technique to the 16/10/15, 13:05:42 UT - 13:06:04 UT period (multi-colored curve on the right) in comparison with that of two hand-made sketches of the s/c path on a larger scale (left and central sketches). The AC refers to the path included within the red squares drawn on both the hand made sketches. The left sketch is adapted from (Burch et al., 2016c) and was inferred from the MMS observations in combination with a 2D PIC numerical simulation. The sketch in the center is drawn using the instantaneous orientations of the MDD normal (purple arrows) with respect to the local magnetic field and the Shue magnetopause model (Shue et al., 1997). All the three drawings have the magnetosphere on the left, the magnetosheath on the right and the *MP* located approximately at their center. The color code of the AC indicates the GSE  $B_z$  component (positive/red within the magnetosphere and negative/blue within the magnetosheath) and the black and the purple arrows departing from the curve at regular intervals indicate the local directions of, respectively, the magnetic field and the MDD normals. We observe that

1. the mutual orientations of  $\mathbf{B}$  and  $\mathbf{n}$  from the AC are almost perpendicular everywhere as expected since the remoteness of the reconnection point (cf. the left and

- the central sketches) suggests that  $B_n$  should be small (*i.e.* the MP should be close to a tangential discontinuity);
2. the AC and the MDD-normal-driven sketches
    - (a) look very similar;
    - (b) agree in describing the back and forth motion already shown in panel 6.c of Figure (6);
    - (c) suggest a more complex motion of the  $s/c$  relative to the  $MP$  than that sketched in the hand made sketch of (Burch et al., 2016c) and
    - (d) show a local  $MP$  curvature opposite to the global curvature of the magnetospheric boundary ( this is at a much smaller scale: tenths of km instead of tens of thousands km).

### 3.2.2 Case study II: spatial profiles compared to time series

On the morning of the same day of case study I, between 10:36:55 and 10:37:50 UT, a crossing occurred that shows clearly that visualization of spacecraft data as a function of time can be misleading. Our analysis of this event is shown in Figure (9). There, the same data have been plotted twice: once as function of time (left column) and once as a function of space (right column). The different rows of panels show: the GSE magnetic field (panels 9.a and 9.a\*); the ion spectrograms where the local maxima with respect to energy have been marked at each time by black points (panels 9.b and 9.b\*); the ion temperatures (panels 9.c and 9.c\*); the electron temperatures (panels 9.d and 9.d\*); the bulk velocity for ions (panels 9.e and 9.e\*) and for electrons (panels 9.f and 9.f\*). We make the following observations:

1. quantitative measures:
  - (a) The length scale of the magnetic field gradient is  $500\text{km} \simeq 6.5d_{i,MSH}$  (see panel 9.a\*); this value agrees both with case study I and the typical magnetopause thickness based on statistical studies (Berchem & Russell, 1982);
  - (b) The magnetic field gradient is significantly displaced to the right compared to the region of the largest variations in the particles (compare panel 9.a\* with respect to panel 9.b\*, 9.c\*, 9.d\*, 9.e\* and 9.f\*);
  - (c) The low energy magnetosheath plasma and the high energy magnetospheric plasma mix in a  $\sim 1d_{i,MSH} \sim 100$  km thick sub layer (observe the black points in the panel 9.b\*).
2. qualitative considerations:
  - (a) The spatial profiles of the ion and the electron temperatures appear approximately monotonic while the temporal ones do not (cf. panels 9.c and 9.d with respect to panels 9.c\* and 9.d\*);
  - (b) The feature that looks like a multiple electron beam (panel panels 9.f, between 12s and 16.5s) is actually one electron beam probed multiple times (panel panels 9.f\*, between  $X_N = 200\text{km}$  and  $300\text{km}$ ).

Here, as well as for the case study analysed in section (3.2.1), the  $\partial_{t,0}\mathbf{B}$  term is negligible with respect to the observed  $\partial_{t,sc}\mathbf{B}$  term and the computed  $\partial_{t,0}\mathbf{X} \cdot \nabla\mathbf{B}$  term.

## 4 Conclusions

In this paper we discuss methods to compute spacecraft ( $s/c$ ) trajectories across weak-stationary plasma structures ( $PSs$ ). We present two new methods (SVF, section 2.1.3 and MVF, section 2.1.2) conceived for the computation of the  $s/c$  velocity with respect to the  $PS$  and therefore useful to find a  $s/c$  path by temporal integration. These

methods allow us to observe the *PS* kinematics and the details of its internal structures avoiding the assumption of strict stationarity, *i.e.* when the *PS* itself can be subjected to weak modifications during the crossing. By using data provided by MMS crossing the Earth's *MP*, we have been able to determine features down to temporal and spatial scales  $\sim 5 \times 10^{-3}$  times smaller than, respectively, the time period needed by MMS to cross the *MP* and the *MP* thickness.

The methods are first tested on artificial data mimicking an MMS crossing of a stationary 1D *MP*. Both constant velocity and back-and-forth motions of the *s/c* relative to the artificial *MP* are examined (sections 3.1.1 and 3.1.2). Since the artificial *MP* is precisely stationary (time independent), the results of both the new methods agree with those of an improved version of the STD method (Shi et al., 2006) (which we called STD<sup>+</sup>) specifically modified to deal with problems of singularities affecting the original STD.

The SVF and MVF methods are then applied to two real *MP* crossings observed by MMS on 16 October 2015. The calculated *s/c* paths are first limited to 1D projections along the normal to the *MP* due to a common intrinsic inaccuracy of the three methods (SVF, MVF and STD<sup>+</sup>) in computing the magnetic field structure velocity along the tangential directions. Nevertheless these results (section 3.2) lead to detailed informations about the kinematics and the thickness of the *MP* structure. Regarding the 13:05:30+60s crossing (case study I, section 3.2.1) the displacements  $X_N(t)$  resulting from the SVF, MVF and STD<sup>+</sup> methods agree with each other in describing a back-and-forth motion of the *MP*, as indicated also by previous studies (Rezeau et al., 2018) but with less accuracy. The fundamental importance of the time-to-space translation of the *s/c* data is ultimately underlined by the analysis performed for the 10:36:55 + 55s crossing (case study II, section 3.2.2). The analysis of this crossing by means of our techniques allows us to determine 1) the position and the extension of the layer where the magnetosheath and the magnetospheric plasmas actually mix, 2) the spatial profiles of the different quantities that mark the *MP* boundary and 3) the exact attribution of multiple signatures to plasma structures that are probed multiple times because back-and-forth motions.

Finally, thanks to the particular conditions occurring during the 13:05:30+60s crossing (section 3.2.1), a 2D reconstruction of the *s/c* path gives a more detailed picture of the motion of the *s/c* relative to the *MP* than that of hand-made reconstructions (Burch et al., 2016c). The weak assumptions and the optimisation procedures used to set the parameters used by these methods (sections 2.3 and Appendixes) make the results of the SVF and MVF methods reproducible and unbiased by any strong assumptions about the *PS*s and/or by any non-objective decision about the input parameters needed to analyse data.

The SVF and the MVF methods open new possibilities to exploit the ability of multi-spacecraft missions to discriminate temporal from spatial dependencies of observed *PS*s. For any quantity  $\mathbf{Q}$ , they allow distinguishing the two kinds of contributions in its variations: 1) the advection of  $\mathbf{Q}$  due to the bulk motion of the *PS* with respect to the *s/c* and 2) the purely temporal variations of  $\mathbf{Q}$ . The methods therefore allow independent computations of the spatial profiles of different quantities  $\mathbf{Q}$  across the *MP*. Therefore, they can be used to better understand the real dispositions and thicknesses of the several kinds of sub-structures that may be the elements of the *MP*, without *a priori* assumptions, giving a better access to the phenomena at play. Used as inputs in the reconstruction techniques, these methods should help to improve their results. Used as inputs for numerical simulations, they should help in getting more realistic initial conditions. The SVF and MVF methods could also be fruitfully used in turbulence studies for testing the Taylor's Hypothesis (Taylor, 1938) with multi-*s/c* missions.

## A Appendices

### A.1 The optimization of fit periods

The SVF and the MVF methods use linear fits performed with small sequences of data points. As we discussed in the text (section 2.1.2), each fit uses  $p$  points where  $p_{min} \leq p \leq p_{max}$ , and  $p_{min}$  and  $p_{max}$  are found from Equation (5). In the following, we describe the operative algorithm we implemented to set dynamically the parameter  $p$  all along the examined interval in order to cut it into sub-intervals of unequal lengths where the linear fits are the best possible.

Let  $N$  be the total number of data points in the total interval to be examined. This interval is divided into two sub-intervals with one point  $i$  in common. This point belongs to the interval  $[p_{min}, N - p_{min}]$  and there are therefore  $N - 2p_{min}$  possibilities for  $i$ . For each possible value of  $i$ , the linear fits are performed over the two sub-intervals and the corresponding error  $D_i$  is recorded. The curve  $D = \{D_i, \text{ with } i \in [p_{min}, N - p_{min}]\}$  has an absolute minimum for some  $i_{min0}$ , which is the value of  $i$  for which the error is minimized when fitting the entire interval by two straight lines. The point  $i_{min0}$  is therefore taken as a fixed boundary for the next iteration. The second iteration works as the previous one but applied to each of the two intervals  $[0, i_{min0}]$  and  $(i_{min0}, N]$ . The result is that the whole interval is so divided into four sub-intervals:  $[0, i_{min1}]$ ,  $(i_{min1}, i_{min0}]$ ,  $(i_{min0}, i_{min2}]$ ,  $(i_{min2}, N]$ , where  $i_{min1}$  and  $i_{min2}$  are the new fixed boundaries for which the error in fitting the entire period  $[0, N]$  by four straight lines is minimized. The procedure is so repeated until there are no more divisions are allowed since there are no more intervals longer than  $p_{max}$  points.

### A.2 The GDMC method

The  $STD^+$ , the SVF and the MVF methods depend on some thresholds that define the minimum quality of the fits to be retained ( $D_{lim,SVF}$  and  $D_{lim,MVF}$ ) and the minimum  $MP$  properties ( $K_{1D}$  and  $K_{dtB}$ ) for which the methods are valid. In order to set these parameters automatically, we use a gradient-directed Monte Carlo Approach (GDMC, see section (2.3)) to find the thresholds that make the displacements  $X_N(t)$  for SVF and MVF as close as possible to each other for the longest time period. In section (2.3) we introduced the GDMC approach briefly. Here we explain how we implemented it for our purposes in more details.

We organize the ensemble of thresholds in a vector  $C_r$  (see Equation 9) that represents a general state in a 4D phase space  $\mathcal{F}_{C_r}$ . The goal is to find the particular  $C_r^*$  that minimizes the distance between the displacements  $X_N(t)$  of the SVF and MVF methods for the maximum amount of time. The resulting  $K_{1D}$  and  $K_{dtB}$  parameters are so used to evaluate the  $X_N(t)$  displacement according to the  $STD^+$  method too.

For a particular crossing, the optimization algorithm proceeds as follows:

1. We manually define a starting  $C_r^*$  usually having  $K_{1D} \leq 1$  and  $K_{dtB} \simeq D_{lim,SVF} \simeq D_{lim,MVF} \ll 1$ ;
2. Then the following operations are iterated (iteration index:  $i$ ):
  - (a) A population  $\Lambda_i$  of  $C_r$ s is generated, each deviating from  $C_r^*$  by a relatively small variation  $\epsilon$  of one (or more than one) of its components (note:  $\Lambda_i$  occupies a sub region  $f^i \in \mathcal{F}_{C_r}$ );
  - (b) The SVF and MVF methods are applied to the same data set for every  $C_r \in \Lambda_i$ . All the  $C_r$  of this ensemble are sorted according to a fitness function  $F(C_r)$  that evaluates the closeness of  $X_N^{SVF}(t)$  and  $X_N^{MVF}(t)$  (see later, Equation (A.1));



- (c) A new sub-region  $f^{i+1} \in \mathcal{F}_{C_r}$  is individuated by a procedure explained hereafter, allowing to extrapolate the trend of the best  $C_r$ s  $\in \Lambda_i$  in the direction where the fitness function is surmised to be minimized;
- (d) If  $f^{i+1} \neq f^i$  a new population  $\Lambda_{i+1}$  is generated sampling randomly the sub-space  $f^{i+1}$  and the previous instructions are repeated. Otherwise, the target is selected between the highest ranked  $C_r$ s  $\in \Lambda_i \in f^i$ .

The above algorithm therefore looks for a minimum of  $F(C_r)$  in  $\mathcal{F}_{C_r}$ , by sampling new possible candidates, at each iteration, in the direction given by  $-\bar{\nabla}F(C_r)$  (until  $\bar{\nabla}F(C_r) \simeq 0$ ).

Now we explain 1) how we defined the fitness function  $F(C_r)$  and 2) how a new population  $\Lambda_{i+1}$  is generated learning from the errors made by the population  $\Lambda_i$ :

1. The fitness function  $F$  judges each  $C_r$  according to the following criteria:

- (a) The closer the  $X_N$  displacements are for SVF and MVF, the better the  $C_r$  is and
- (b) The longer the time period for which  $X_N$  can be calculated for both SVF and MVF is, the better the  $C_r$  is.

Therefore we define the fitness function as a linear combination of the ranks  $r_{\Delta X_N}$  and  $r_{\Delta t}$  with which a particular  $C_r^* \in \Lambda_i$  is classified in comparison with the others  $C_r \in \Lambda_i$  according to, respectively, the total distance between the displacements  $X_N$  and the extension of the time period during which both the displacements can be computed:

$$F(C_r) \equiv k_{\Delta X_N} r_{\Delta X_N}(C_r) + k_{\Delta t} r_{\Delta t}(C_r) \quad (\text{A.1})$$

Both  $r_{\Delta X_N}$  and  $r_{\Delta t}$  are integer values  $\in [1, \text{card}(\Lambda_i)]$  with 1 for the best result and  $\text{card}(\Lambda_i)$  for the worst. Here both the weights  $k_{\Delta X_N}$  and  $k_{\Delta t}$  are set to 1, the two ranking criteria being of equal importance.

2. The procedure for generating a new population  $\Lambda_{i+1}$  is governed by the gradient of  $F(C_r)$ , where  $C_r \in \Lambda_i$ . A sub-set of  $C_r$  is first determined, gathering the best ranked vectors. Then, for each component  $m$  of  $C_r$  in this sub-set, a linear fit is performed and this trend is extrapolated in the direction that minimizes  $F$ . The  $m^{\text{th}}$  component of the new set  $f^{i+1}$  is then chosen around this extrapolated trend. The new population  $\Lambda_{i+1}$  is finally randomly chosen in the new sub-region  $f^{i+1}$ . The number of the best-ranked  $C_r$ s to be fitted, the extension of the extrapolation and the random generation of the new elements around the extrapolated trend are details to be set according to a preliminary analysis. Anyway, they do not influence the shape of the displacements  $X_N$  but only the speed of convergence of the optimization process. This procedure, likewise the cross-over procedure adopted by the genetic algorithms (GA, (Holland, 1992)), allows one to modify ongoing the sub-regions  $f \in \mathcal{F}_{C_r}$  but, in contrast to GAs, it allows one to take into account a smaller initial population  $\Lambda_{i=0}$  (good for reducing computational cost) since, at the generation  $i > 0$ , it allows to generate  $C_r$ s that are not already produced by some crossing-over combination of the  $C_r \in \Lambda_0$ . In some sense, the GDMC approach can be seen as a GA with two main differences: it is applied to an optimization problem where the parameters to be found are continuous variables and its mutation rate (Holland, 1992) has been pushed to its maximum (which is otherwise very low in GAs).

Figure (A.1) illustrates the optimization procedure. It concerns the 1<sup>st</sup> component of  $C_r$  (*i.e.*  $D_{lim,SVF}$ ) in the case of the real crossing studied in section 3.2.1. Each of the three panels represents one iteration ( $i = \{0, 20, 40\}$ ). Panel A.1.a represents the starting panels step: a population  $\Lambda_0$  of 250  $C_r$ s is randomly generated and all the 1<sup>st</sup> components (blue "+" ) are sorted by means of the fitness function

$F$  (Equation A.1). We observe that the points having the best rank show a clear trend (see the green line which is the fit of the first 70 best ranked elements). The red dashed line extrapolates this trend to a region where the elements are expected to get better ranks if they were taken into account. Therefore, a new population  $\Lambda_1$  of possible  $D_{lim,SVF}$  are randomly generated around the red dashed line and ranked according to Equation (A.1) (orange "x"). The generation procedure maintains the number of  $C_r$  constant and all new components are chosen with positive ordinates since negative values of  $D_{lim,SVF}$  are meaningless. After 20 generations (panel A.1.b), both the spread of the points and the slope of their fit have decreased: the algorithm is converging. As a matter of fact, at generation 40 (panel A.1.c), all the  $D_{lim,SVF}$  values  $\in \Lambda_{40}$  are located in a small region near  $\sim 1.7$  and the next -randomly generated- values of  $D_{lim,SVF} \in \Lambda_{41}$  shares the same region: the algorithm has so converged.

## Acknowledgments

The authors thank Laurent Mirioni for his help in dealing with the MMS data and for fruitful discussions. The French involvement on MMS is supported by CNES and CNRS. Work at Dartmouth College was supported by NASA grant 80NSSC19K0254. All the data used are available on the MMS data server: <https://lasp.colorado.edu/mms/sdc/public/about/browse-wrapper/>.

## References

- Berchem, J., & Russell, C. T. (1982). The thickness of the magnetopause current layer: Isee 1 and 2 observations. *Journal of Geophysical Research: Space Physics*, 87(A4), 2108–2114. doi: 10.1029/JA087iA04p02108
- Burch, J. L., Moore, T. E., Torbert, R. B., & Giles, B. L. (2016b). Magnetospheric multiscale overview and science objectives. *Space Science Reviews*, 199(1), 5–21. doi: 10.1007/s11214-015-0164-9
- Burch, J. L., & Torbert, R. B. (2016a). Preface. *Space Science Reviews*, 199(1-4), 1–3. Retrieved from <https://doi.org/10.1007/s11214-015-0153-z> doi: 10.1007/s11214-015-0153-z
- Burch, J. L., Torbert, R. B., Phan, T. D., Chen, L.-J., Moore, T. E., Ergun, R. E., ... Chandler, M. (2016c). Electron-scale measurements of magnetic reconnection in space. *Science*, 352, aaf2939. doi: 10.1126/science.aaf2939
- Chanteur, G. (1998). Spatial Interpolation for Four Spacecraft: Theory. *ISSI Scientific Reports Series*, 1, 349–370.
- De Keyser, J. (2008). Empirical Reconstruction. *ISSI Scientific Reports Series*, 8, 91–98.
- Denton, R. E., Sonnerup, B. U. Ö., Birn, J., Teh, W.-L., Drake, J. F., Swisdak, M., ... Baumjohann, W. (2010). Test of methods to infer the magnetic reconnection geometry from spacecraft data. *Journal of Geophysical Research*, 115(10). doi: 10.1029/2010JA015420
- Denton, R. E., Sonnerup, B. U. Ö., Russell, C. T., Hasegawa, H., Phan, T.-D., Strangeway, R. J., ... Vines, S. K. (2018). Determining L-M-N current sheet coordinates at the magnetopause From Magnetospheric Multiscale Data. *Journal of Geophysical Research: Space Physics*, 123(3), 2274–2295. doi: 10.1002/2017JA024619
- Dorville, N., Belmont, G., Rezeau, L., Aunai, N., & Retinò, A. (2014b). BV technique for investigating 1-D interfaces. *Journal of Geophysical Research: Space Physics*, 119(3), 1709–1720. doi: 10.1002/2013JA018926
- Dorville, N., Belmont, G., Rezeau, L., Grappin, R., & Retinò, A. (2014a). Rotational/compressional nature of the magnetopause: Application of the BV

- technique on a magnetopause case study. *Journal of Geophysical Research: Space Physics*, 119(3), 1898–1908. doi: 10.1002/2013JA018927
- Escoubet, C., Schmidt, R., & Goldstein, M. (1997). Cluster – science and mission overview. *Space Science Reviews*, 79(1), 11–32. doi: 10.1023/A:1004923124586
- Faganello, M., & Califano, F. (2017). Magnetized Kelvin-Helmholtz instability: theory and simulations in the Earth’s magnetosphere context. *Journal of Plasma Physics*, 83(6). doi: 10.1017/S0022377817000770
- Hasegawa, H., Sonnerup, B. U. ., Denton, R. E., Phan, T.-D., Nakamura, T. K. M., Giles, B. L., . . . Saito, Y. (2017). Reconstruction of the electron diffusion region observed by the Magnetospheric Multiscale spacecraft: First results. *Geophysical Research Letters*, 44(10), 4566–4574. doi: 10.1002/2017GL073163
- Hasegawa, H., Sonnerup, B. U. O., Dunlop, M. W., Balogh, A., Haaland, S. E., Klecker, B., . . . Rème, H. (2004). Reconstruction of two-dimensional magnetopause structures from Cluster observations: verification of method. *Annales Geophysicae*, 22(4), 1251–1266. doi: 10.5194/angeo-22-1251-2004
- Hasegawa, H., Sonnerup, B. U. O., Eriksson, S., Nakamura, T. K. M., & Kawano, H. (2015). Dual-spacecraft reconstruction of a three-dimensional magnetic flux rope at the Earth’s magnetopause. *Annales Geophysicae*, 33(2), 169–184. doi: 10.5194/angeo-33-169-2015
- Hasegawa, H., Sonnerup, B. U. Ö., Hu, Q., & Nakamura, T. (2014). Reconstruction of an evolving magnetic flux rope in the solar wind: Decomposing spatial and temporal variations from single-spacecraft data. *Journal of Geophysical Research: Space Physics*, 119(1), 97–114. doi: 10.1002/2013JA019180
- Hasegawa, H., Sonnerup, B. U. Ö., & Nakamura, T. K. M. (2010). Recovery of time evolution of Grad-Shafranov equilibria from single-spacecraft data: Benchmarking and application to a flux transfer event. *Journal of Geophysical Research: Space Physics*, 115(A11). doi: 10.1029/2010JA015679
- Holland, J. (1992). Genetic Algorithms. *Scientific American*, 267(1). doi: 10.1038/scientificamerican0792-66
- Hu, Q., & Sonnerup, B. U. Ö. (2003). Reconstruction of two-dimensional structures in the magnetopause: Method improvements. *Journal of Geophysical Research: Space Physics*, 108(A1), SMP 9-1-SMP 9-9. doi: 10.1029/2002JA009323
- Hu, X., Beratan, D. N., & Yang, W. (2008). A gradient-directed Monte Carlo approach to molecular design. *The Journal of Chemical Physics*, 129(6), 064102. doi: 10.1063/1.2958255
- Le Contel, O., Retinò, A., Breuillard, H., Mirioni, L., Robert, P., Chasapis, A., . . . Saito, Y. (2016). Whistler mode waves and hall fields detected by mms during a dayside magnetopause crossing. *Geophys. Res. Lett.*, 43(12), 5943–5952. (2016GL068968) doi: 10.1002/2016GL068968
- Rezeau, L., Belmont, G., Manuzzo, R., Aunai, N., & Dargent, J. (2018). Analyzing the Magnetopause Internal Structure: New Possibilities Offered by MMS Tested in a Case Study. *Journal of Geophysical Research: Space Physics*, 227–241. doi: 10.1002/2017JA024526
- Rezeau, L., Roux, A., & Russell, C. T. (1993). Characterization of small-scale structures at the magnetopause from ISEE measurements. *Journal of Geophysical Research: Space Physics*, 98(A1), 179–186. doi: 10.1029/92JA01668
- Shi, Q. Q., Shen, C., Dunlop, M. W., Pu, Z. Y., Zong, Q.-G., Liu, Z. X., . . . Balogh, A. (2006). Motion of observed structures calculated from multi-point magnetic field measurements: Application to Cluster. *Geophys. Res. Lett.*, 33(8), n/a–n/a. (L08109) doi: 10.1029/2005GL025073
- Shi, Q. Q., Shen, C., Pu, Z. Y., Dunlop, M. W., Zong, Q.-G., Zhang, H., . . . Balogh, A. (2005). Dimensional analysis of observed structures using multipoint magnetic field measurements: Application to Cluster. *Geophys. Res. Lett.*, 32, L12105. doi: 10.1029/2005GL022454



- Shi, Q. Q., Tian, A. M., Bai, S. C., Hasegawa, H., Degeling, A. W., Pu, Z. Y., ...  
Liu, Z. Q. (2019, May 28). Dimensionality, coordinate system and refer-  
ence frame for analysis of in-situ space plasma and field data. *Space Science*  
*Reviews*, 215(4), 35. doi: 10.1007/s11214-019-0601-2
- Shue, J.-H., Chao, J. K., Fu, H. C., Russell, C. T., Song, P., Khurana, K. K., &  
Singer, H. J. (1997). A new functional form to study the solar wind control  
of the magnetopause size and shape. *Journal of Geophysical Research: Space*  
*Physics*, 102(A5), 9497–9511. doi: 10.1029/97JA00196
- Sonnerup, B. U. Ö., & Cahill, L. J. (1967). Magnetopause structure and atti-  
tude from Explorer 12 observations. *Journal of Geophysical Research: Space*  
*Physics*, 72(1), 171–183. doi: 10.1029/JZ072i001p00171
- Sonnerup, B. U. Ö., & Hasegawa, H. (2010). On slowly evolving grad-shafranov  
equilibria. *Journal of Geophysical Research: Space Physics*, 115(A11). doi: 10  
.1029/2010JA015678
- Sonnerup, B. U. Ö., Hasegawa, H., Teh, W., & Hau, L. (2006). GradShafranov  
reconstruction: An overview. *Journal of Geophysical Research: Space Physics*  
*(1978–2012)*, 111. doi: 10.1029/2006ja011717
- Taylor, G. I. (1938). The spectrum of turbulence. *Proceedings of the Royal Society of*  
*London. Series A, Mathematical and Physical Sciences*, 164(919), 476–490.
- Torbert, R. B., Burch, J. L., Giles, B. L., Gershman, D., Pollock, C. J., Dorelli, J.,  
... Bounds, S. (2016). Estimates of terms in Ohm’s law during an encounter  
with an electron diffusion region. *Geophys. Res. Lett.*, 43(12), 5918–5925. doi:  
10.1002/2016GL069553

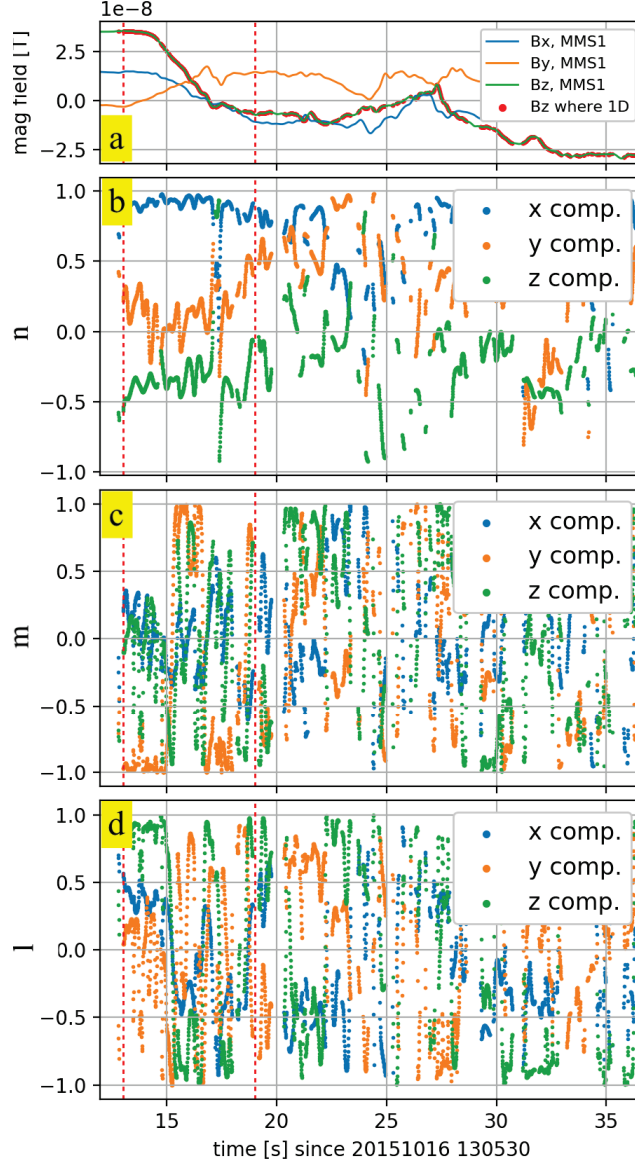


**Figure 1.** GSE components of magnetic field observed by MMS 1 (panel *a*, the sections in red are the times when the structure is 1D), the  $l$ ,  $m$ , and  $n$  components of the  $MP$  frame (panels *b*, *c* and *d*) computed by means of the MDD method (Shi et al., 2005) for 16 October 2015, 13:05:30+60s, using burst mode data (128S/s). Note that the  $m$  and  $l$  directions oscillate rapidly even during times where  $n$  is stable.

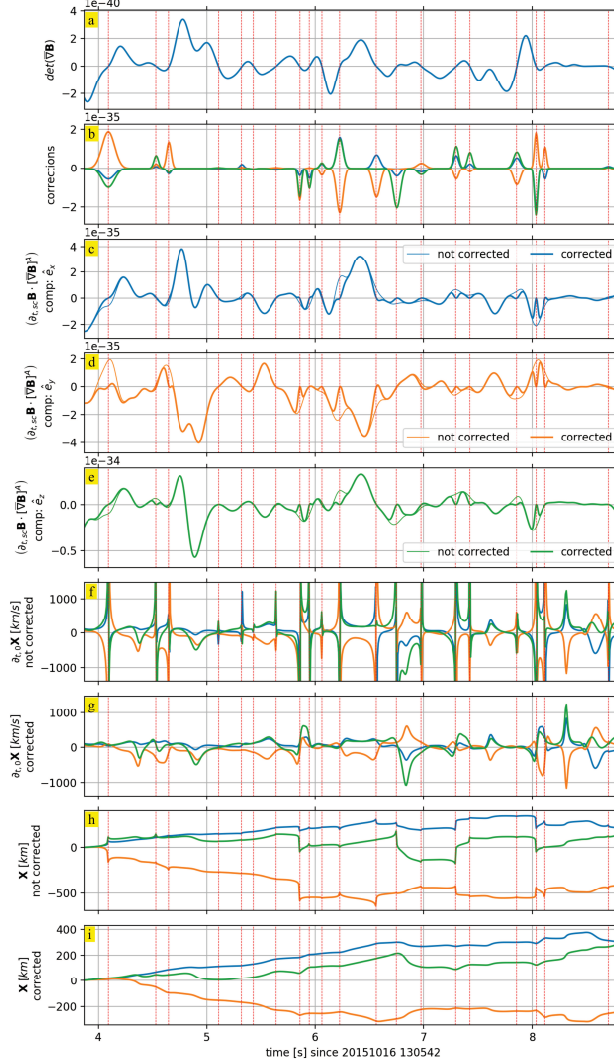


**Figure 2.** Five second zoom for evidencing the origin of the singularities and the way they are corrected. Each component of the calculated velocity is the ratio between a numerator (panels *c*, *d*, and *e* and a denominator (panel *a*), which is the determinant. The denominator cancels at several places which are slightly different from the places where the different numerators cancel (here in GSE frame). This results in singularities, even in the normal coordinate  $V_X$  (panel *f*). If local corrections are applied (panel *b*), these singularities are suppressed (panel *g*) as well as the corresponding jumps in the normal position obtained by integration (panels *h* and *i*).

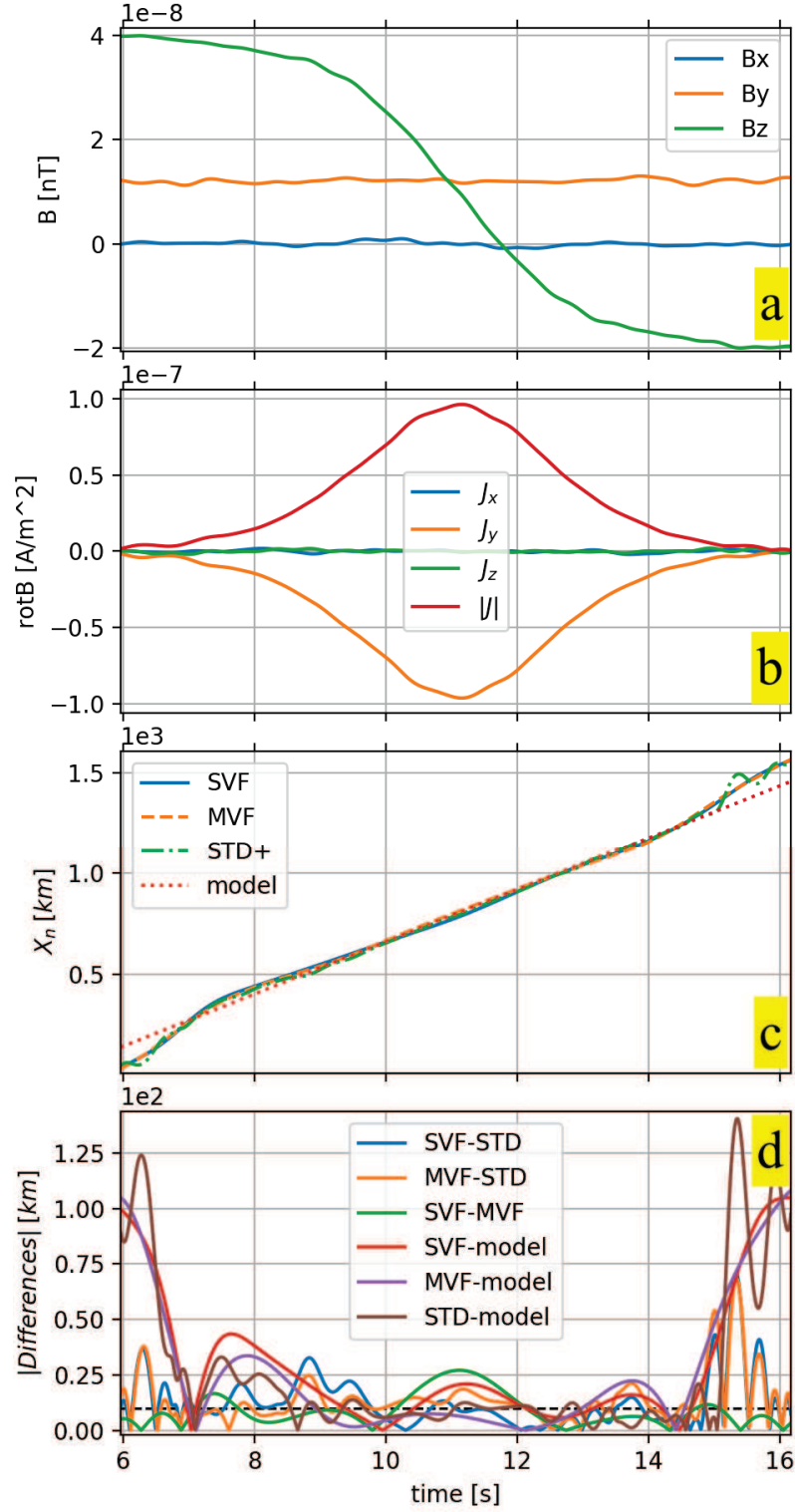


**Figure 3.** Test case I: artificial crossing with constant velocity. Comparison between the STD<sup>+</sup>, SVF and MVF displacements with the exact model (panel c). The magnetic field, the associated curlometer currents and the differences between the displacements are plotted, respectively, in panel a, b and d.

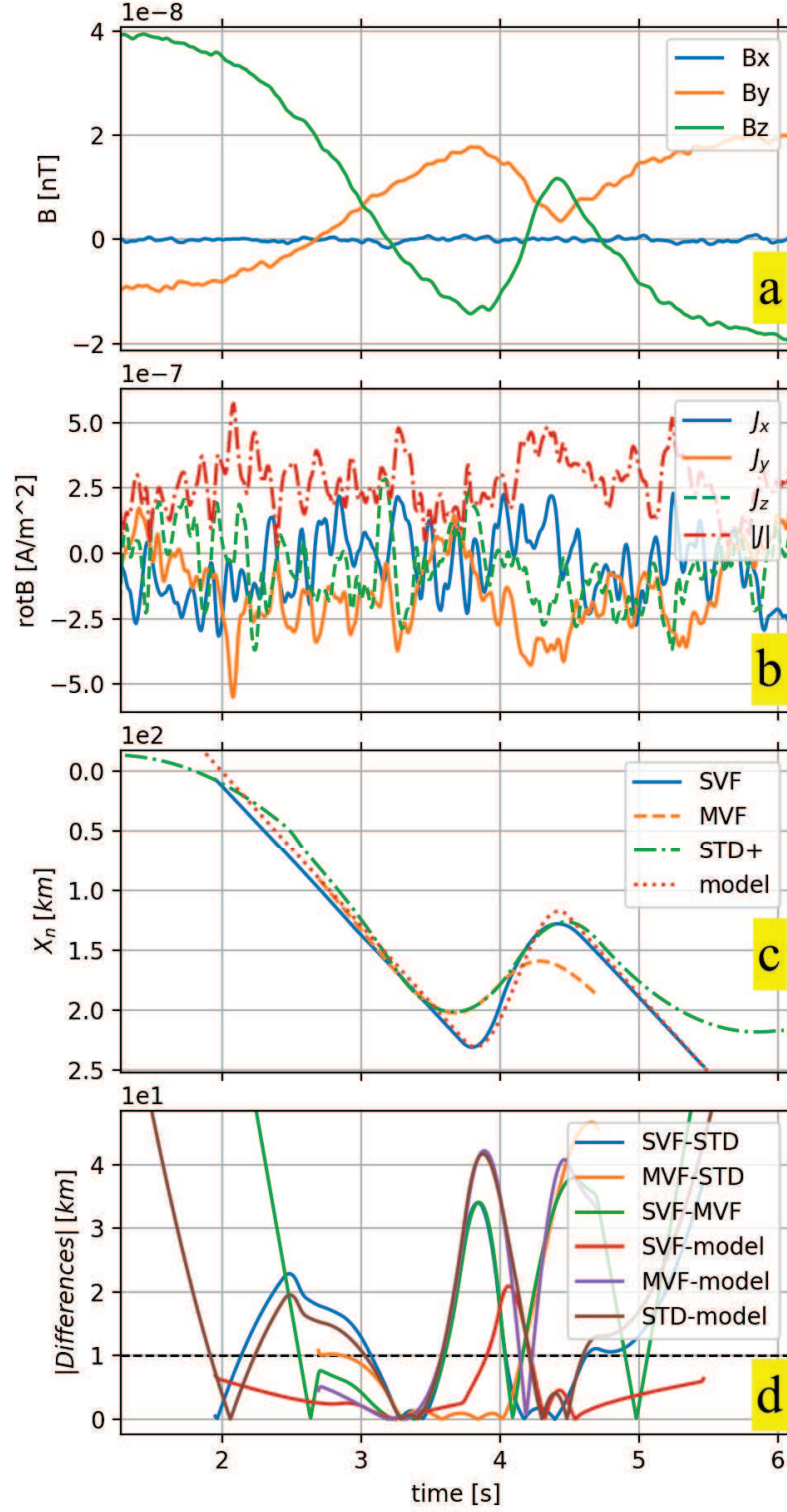
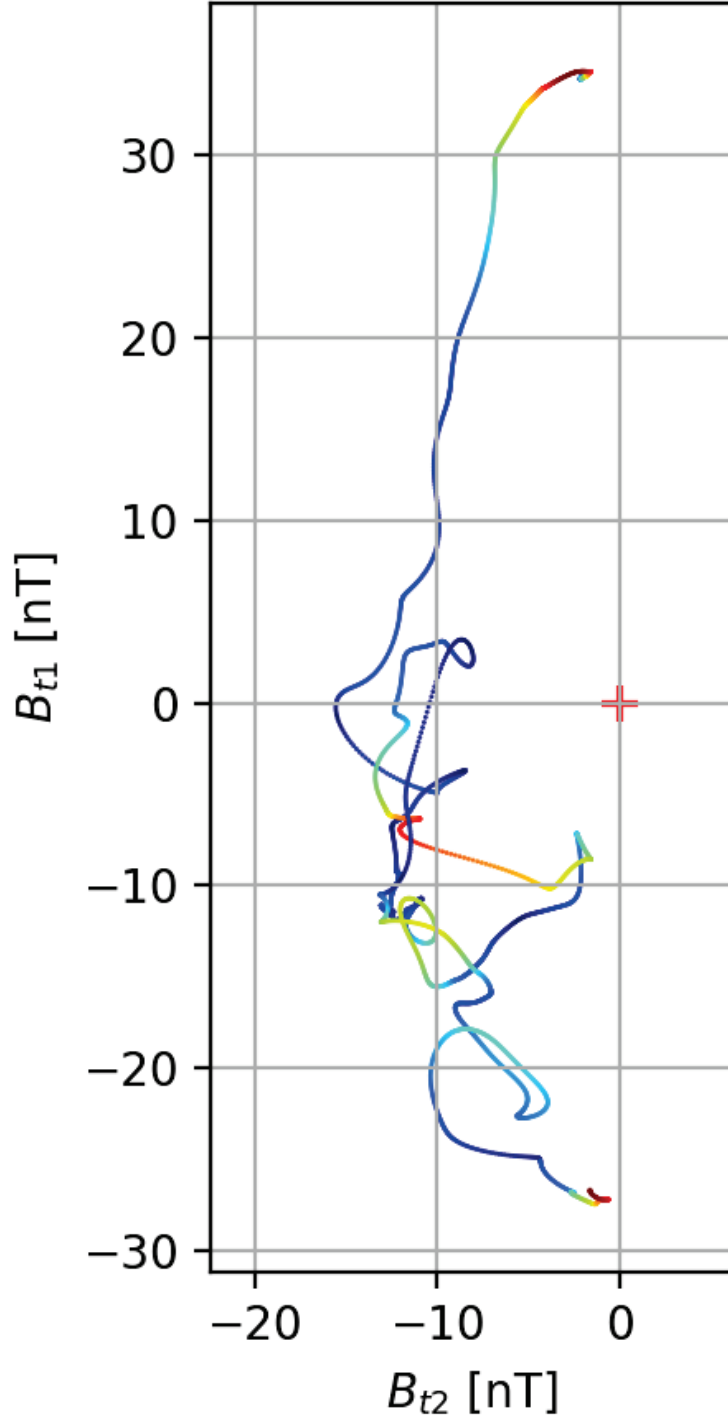


**Figure 4.** Test case II: back and forth crossing. Displacements found using the STD<sup>+</sup>, SVF and MVF methods along with the exact model displacement (panel c). The artificial magnetic field, the associated curlometer currents and the differences between the displacements are plotted, respectively, in panel a, b and d.



535 **Figure 5.** Hodogram of the tangential magnetic field measured by MMS during the 16 Octo-  
 536 ber 2015, 13:05:42+22s crossing. The indexes t1 and t2 refers to the tangential directions used to  
 537 project data (see the text for more details). The color code refers to the magnitude of the normal  
 538 flow crossing the *MP* plotted in panel 6.e of Figure (6).



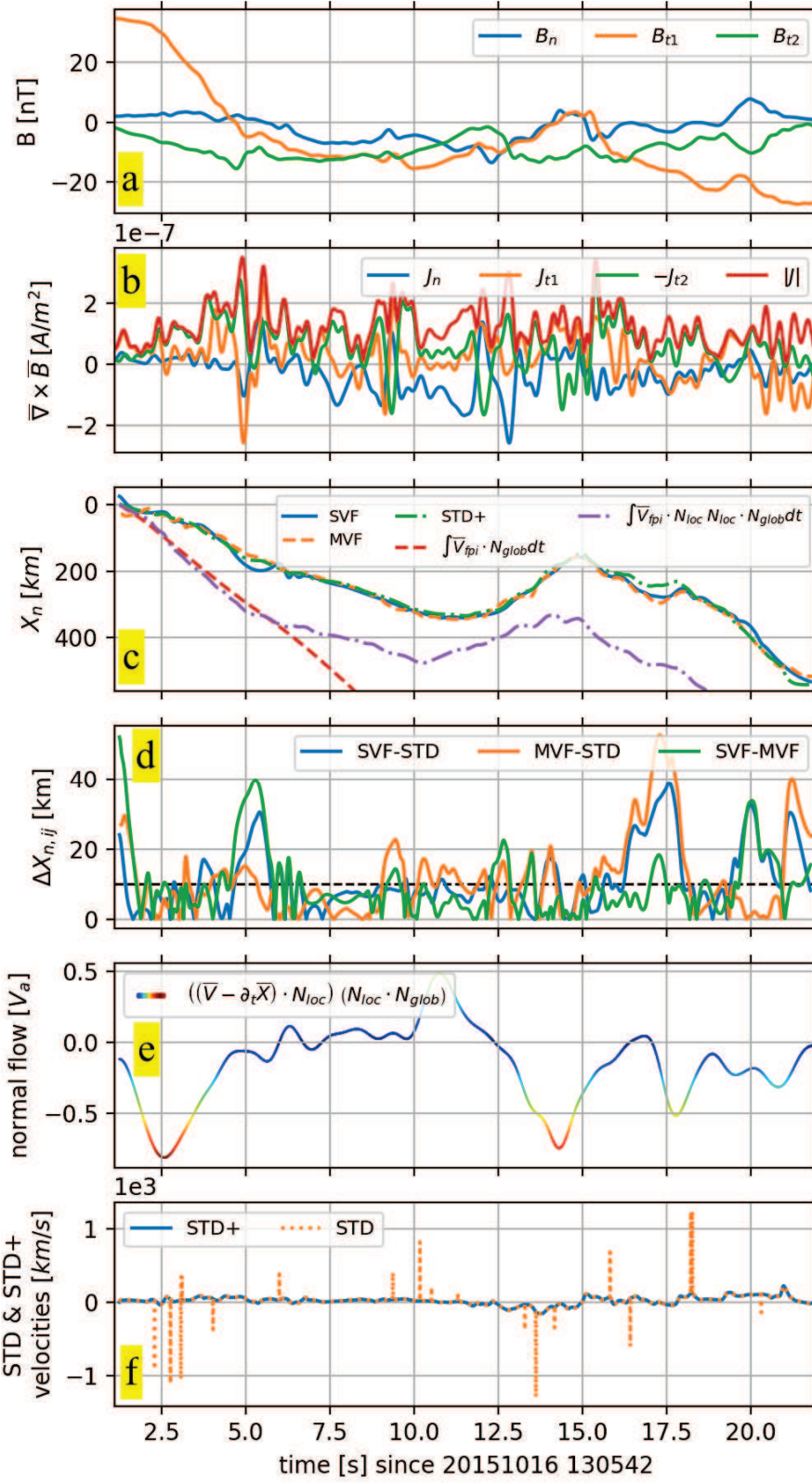


**Figure 6.** Magnetic field (panel a), curlometer current (panel b),  $X_N(t)$  coordinates (panel c),  $\Delta X_{N,ij}$  differences (panel d), residual normal flow (panel e) and comparison between  $|\partial_{t,0}(\mathbf{X}_{STD})|$  and  $|\partial_{t,0}(\mathbf{X}_{STD+})|$  recorded or computed during the 16 October 2015, 13:05:30+60s crossing (here reduced to the 13:05:42+22s window).

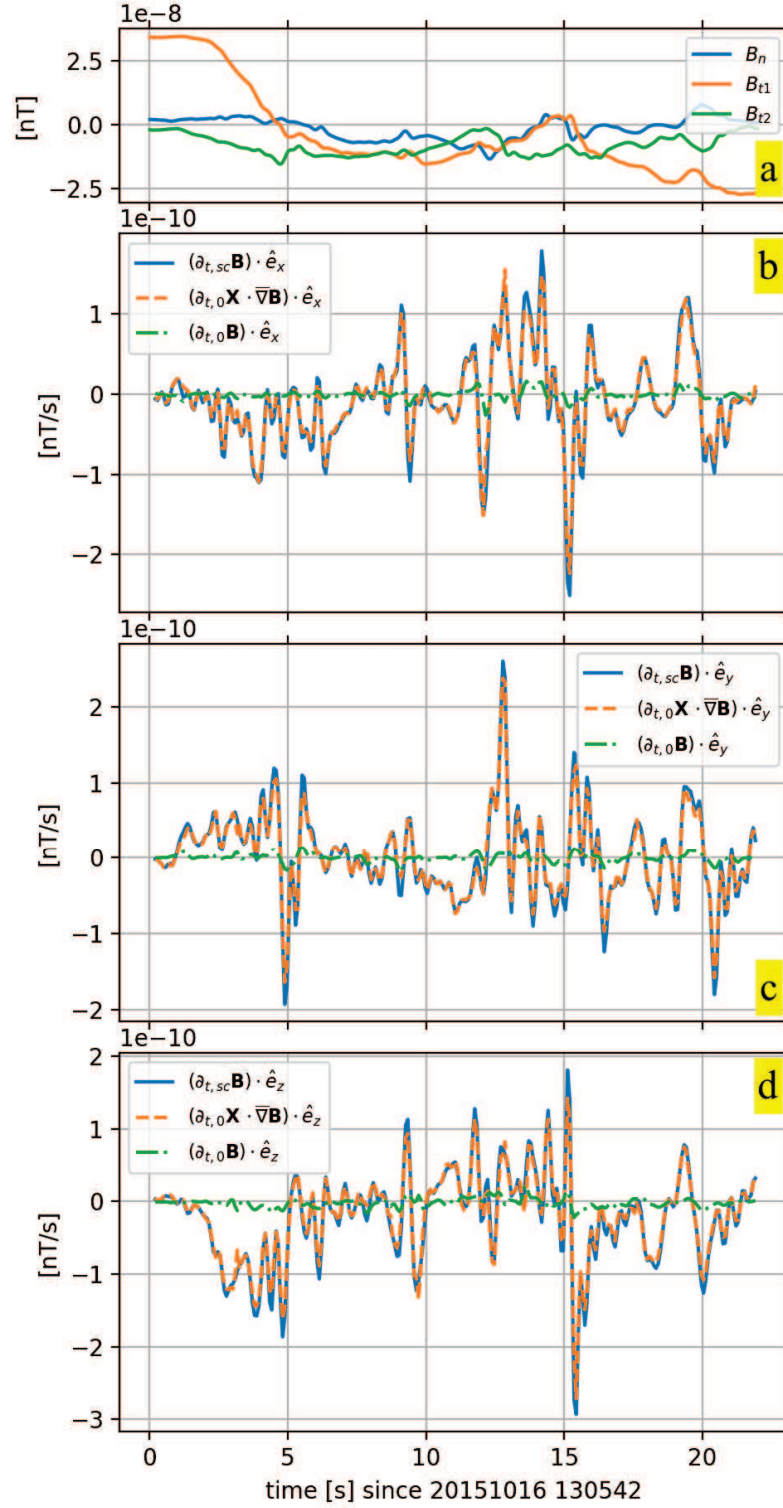


**Figure 7.** Comparison between the terms of Equation (2) (blue =  $\partial_{t,sc}\mathbf{B}$ , orange =  $\partial_{t,0}\mathbf{X} \cdot \nabla\mathbf{B}$  and green =  $\partial_{t,0}\mathbf{B}$  curves) for each of its GSE components (panels b, c and d).



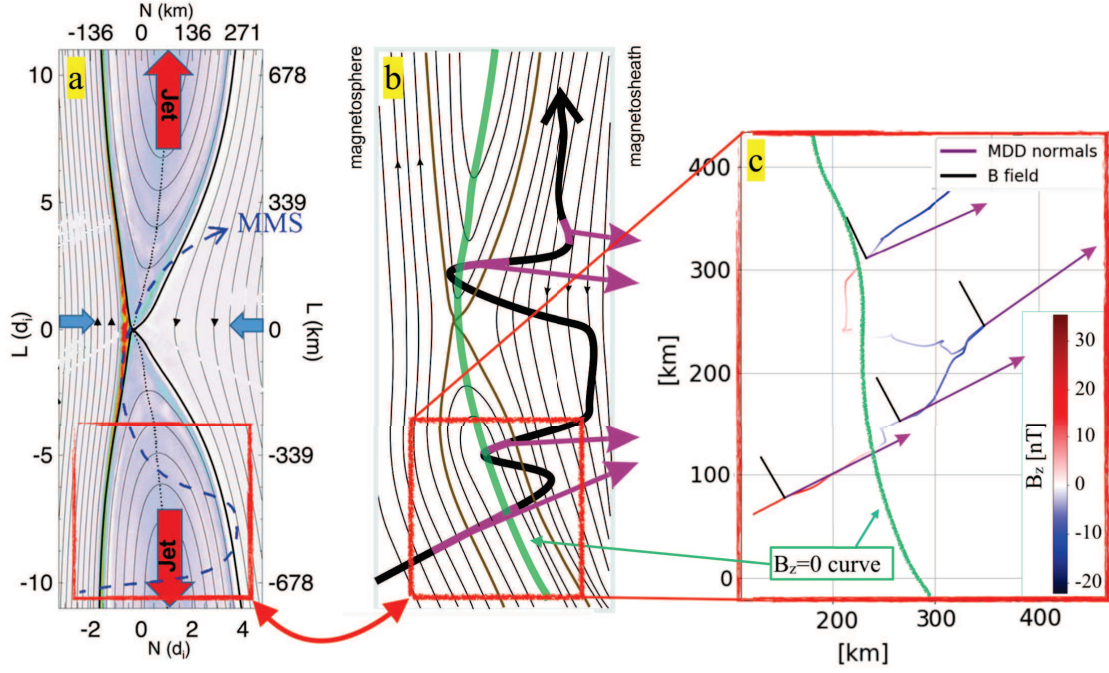


**Figure 8.** Comparison between the hand-made sketch made by (Burch et al., 2016c) (on the left), a hand-made sketch suggested by the relative direction of the MDD normals with respect to the local magnetic field and the Shue model (Shue et al., 1997) (central sketch) and the path obtained automatically by our MVF technique applied on the 16/10/15, 13:05:42 UT - 13:06:04 UT period (on the right). The automatic result concerns the portion of the path enclosed in the red squares drawn on the hand made sketches. In both panels *b* and *c* the green curved lines joining the  $B_z = 0$  points are drawn by hand.

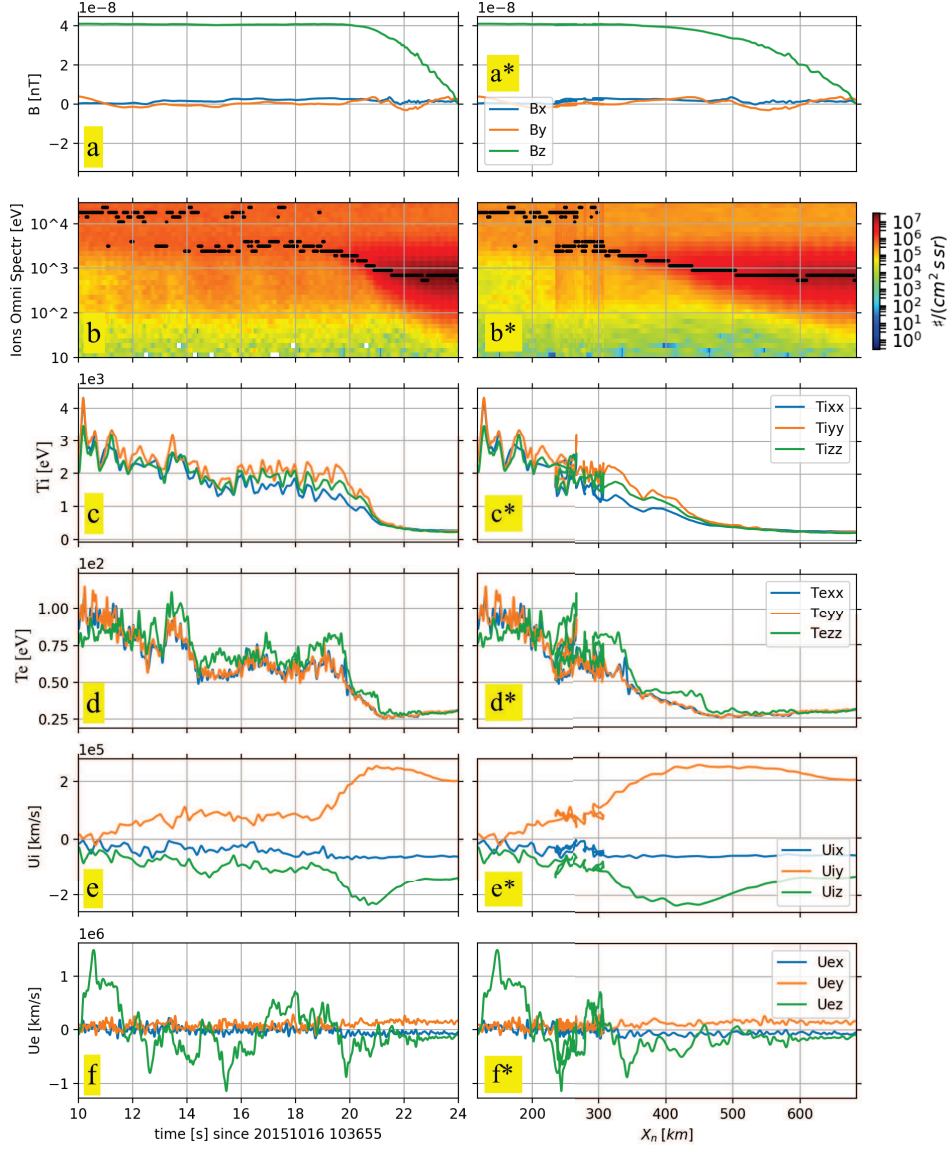


**Figure 9.** Time vs space visualization of some quantities of interest for the case 16/10/2015, 10:36:55 + 55s. The quantities are visualised twice: as a function of time on the left and as a function of space on the right. The figure shows the GSE components of the magnetic field (panels *a* and *a\**), the ions spectrograms and their maxima (panels *b* and *b\**), the ions and electrons temperatures (panels *c*, *c\** and *d*, *d\**), the ions and electrons bulk velocities (panels *e*, *e\** and *f*, *f\**).

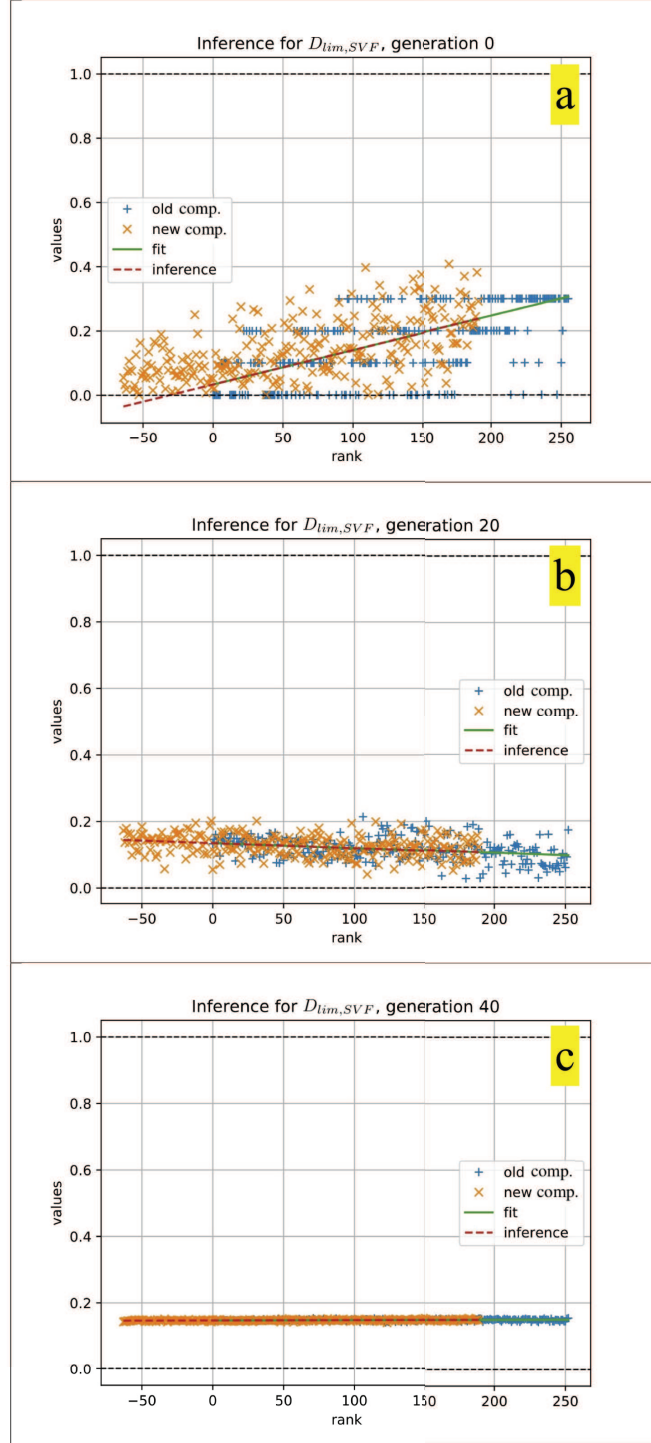


**Figure A.1.** Illustration of the GDMC optimization procedure for determining the threshold  $D_{lim,SVF}$ . Panels *a*, *b* and *c* show three different moments of the convergence process: the begin (panel *a*), the end (panel *c*) and a step in between (panel *b*). Each panel shows the first components of  $C_r(D_{lim,SVF})$  already sorted by means of the fitness function (blue "+"), the fit of the best-classified 70 elements (green line), the extrapolated trend (red dashed line) and the new values randomly generated around the extrapolated trend (orange "X"). Note that the orange points, which are derived from a purely mathematical extrapolation, can go without problem to the negative range of  $x$ , even if negative ranks have no meaning in themselves. On the contrary, the blue points, which are obtained by ranking, always correspond to positive values of  $x$ .

Figure1.

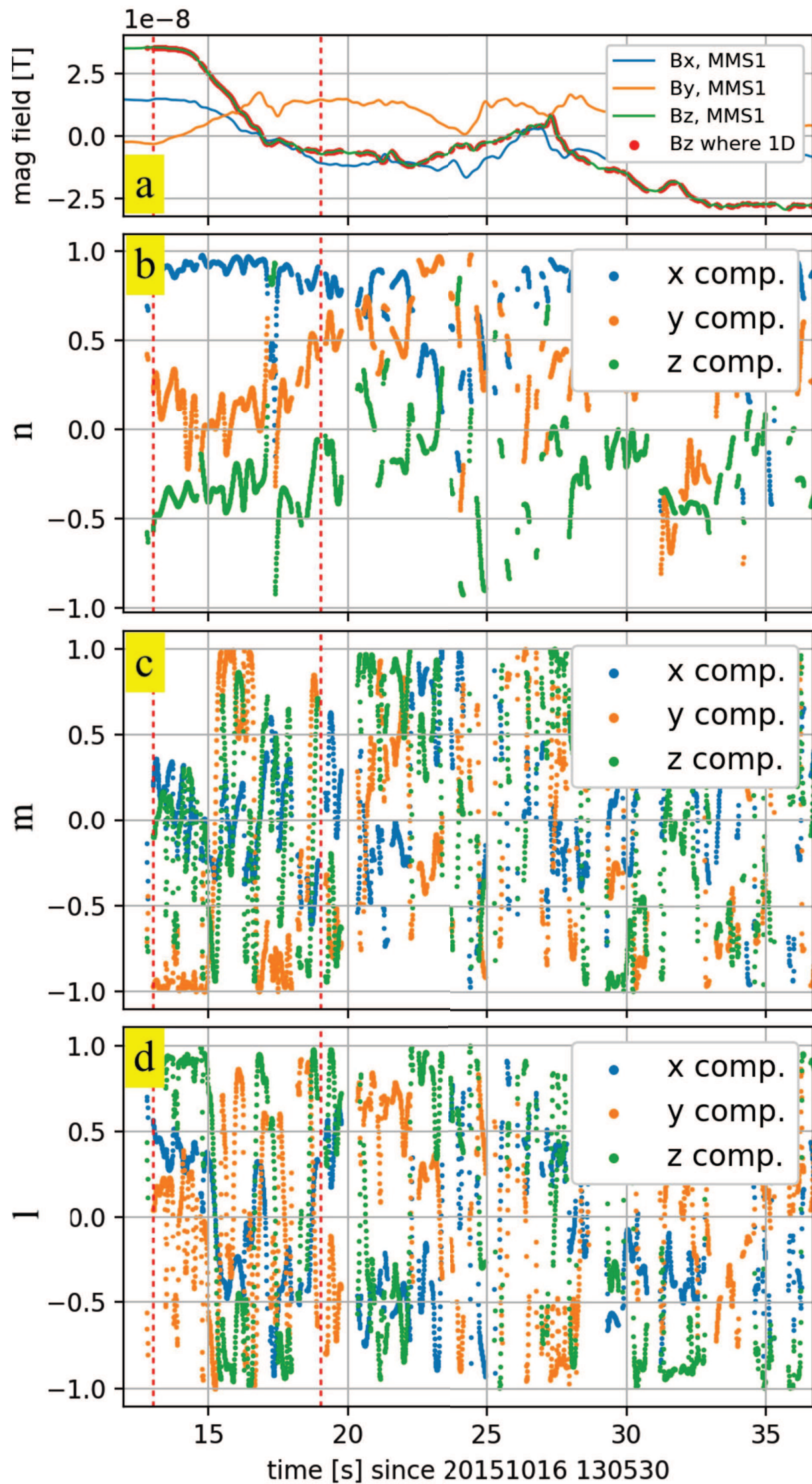


Figure2.



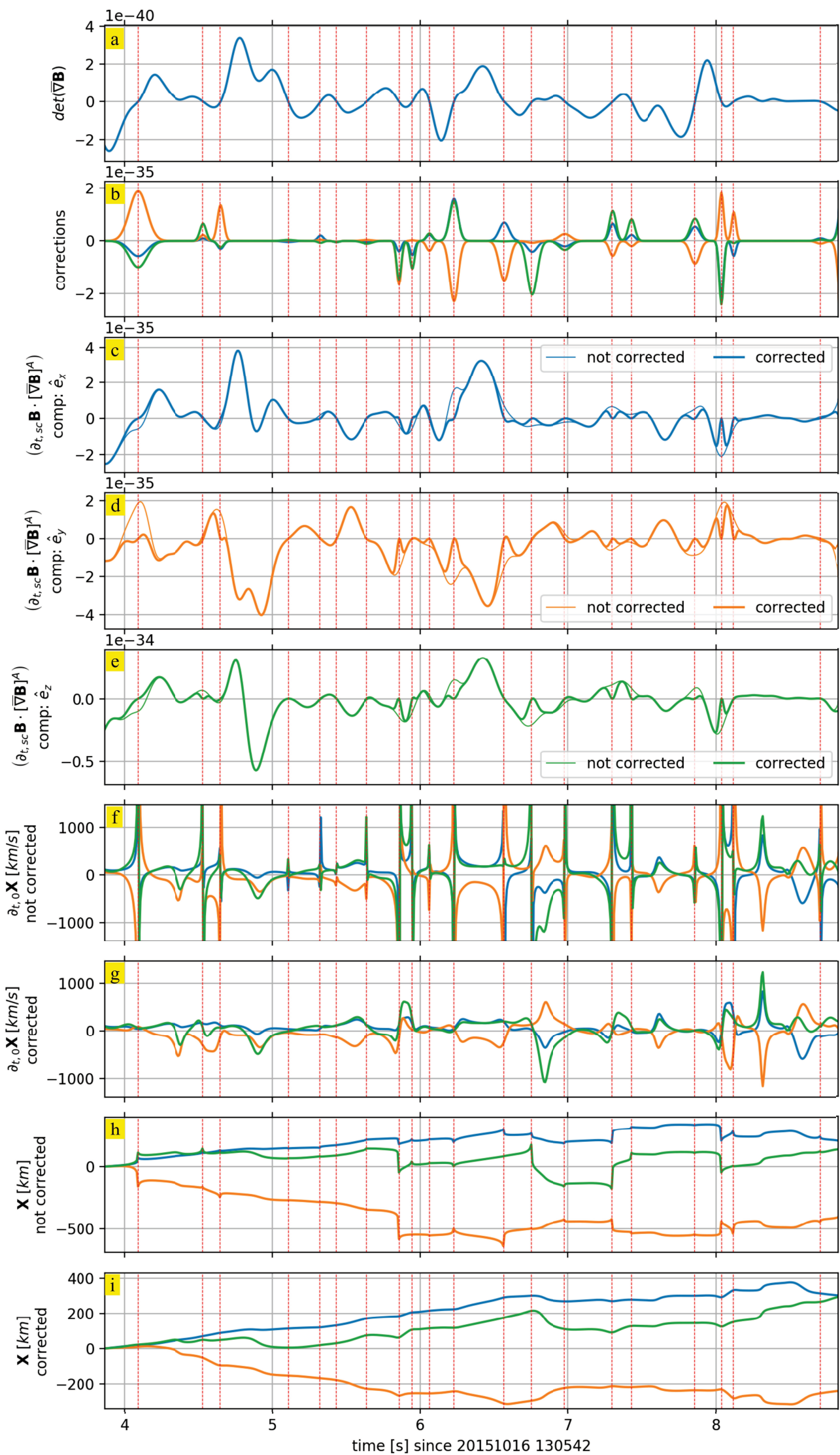


Figure3.



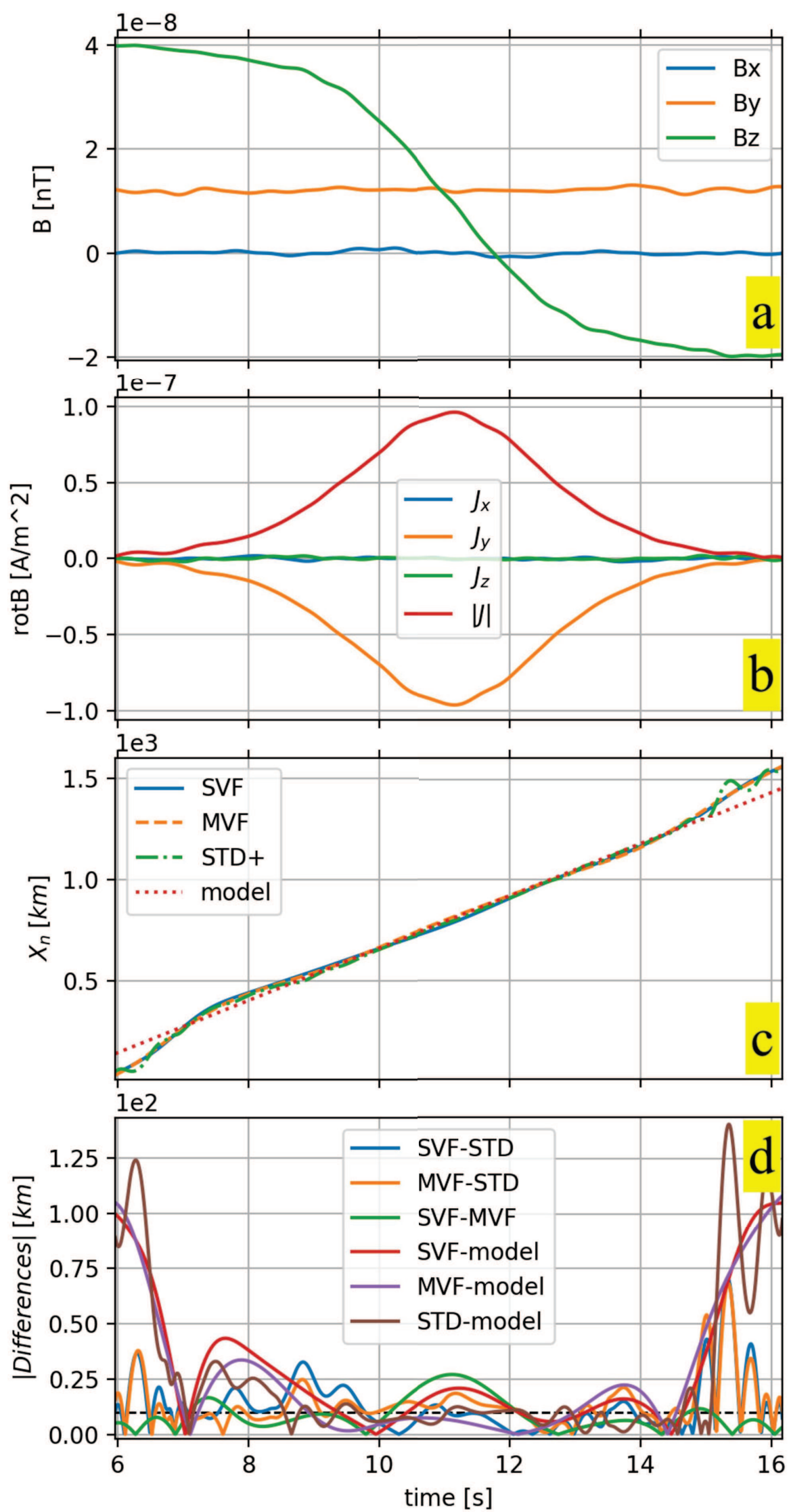


Figure4.

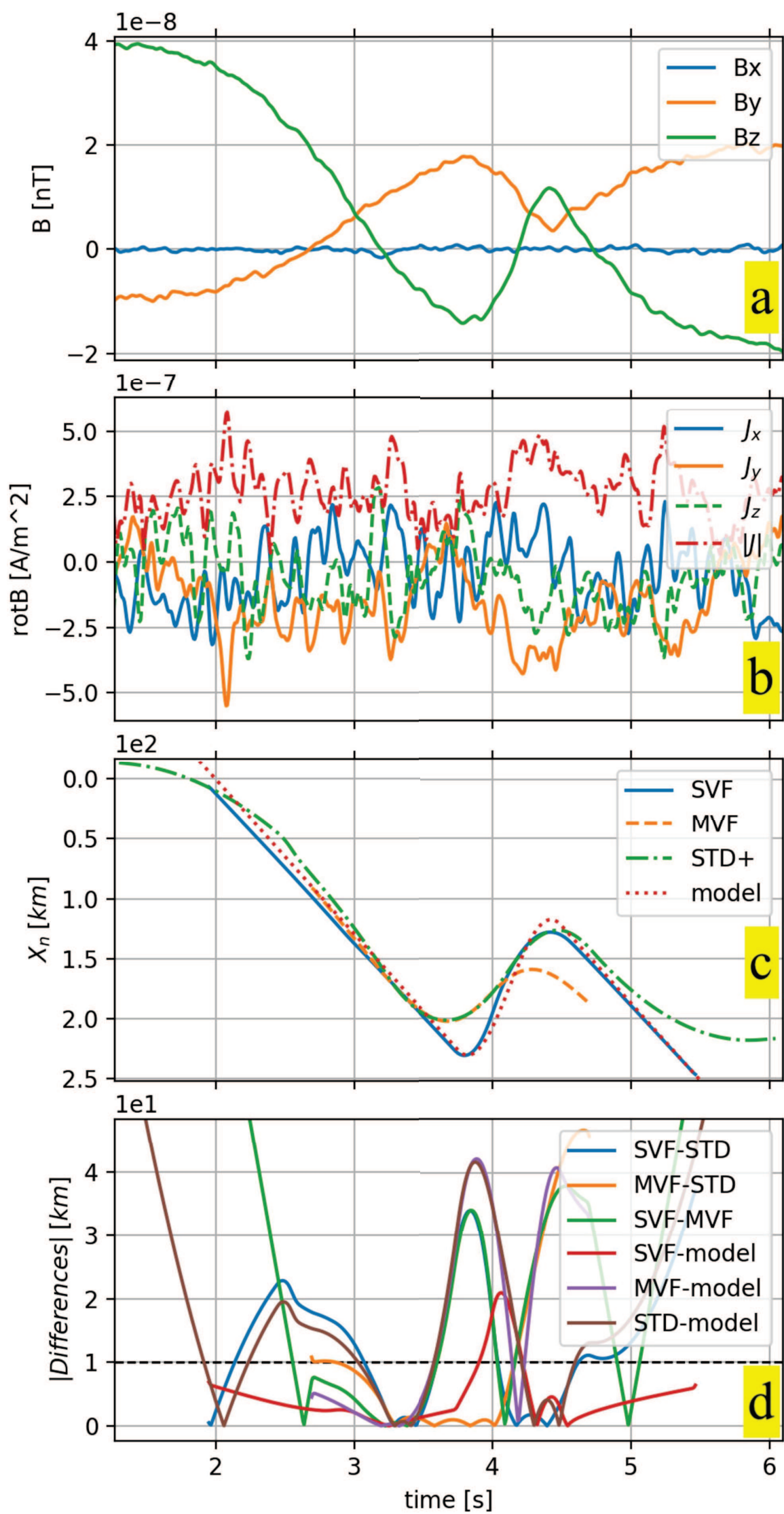


Figure5.

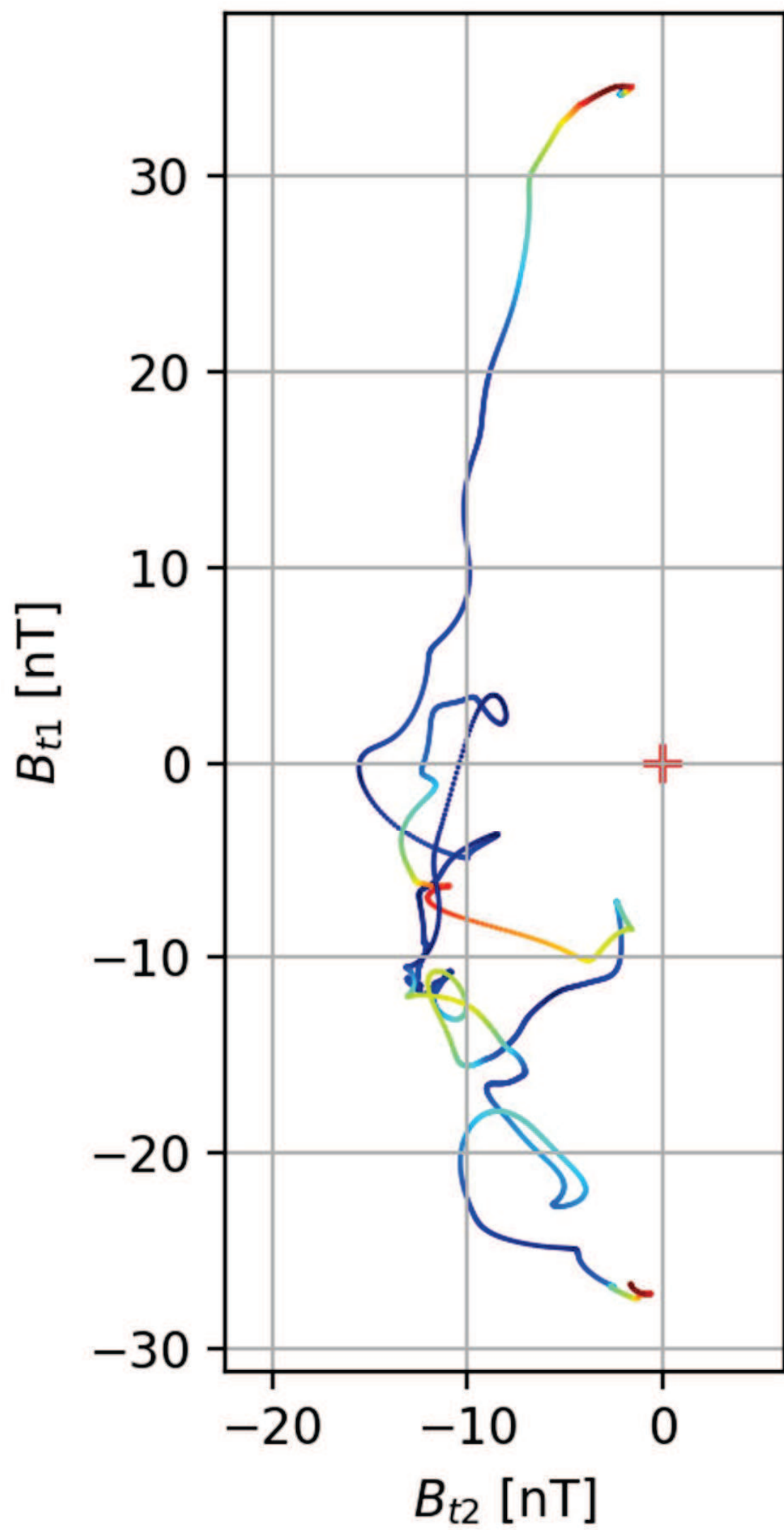


Figure6.



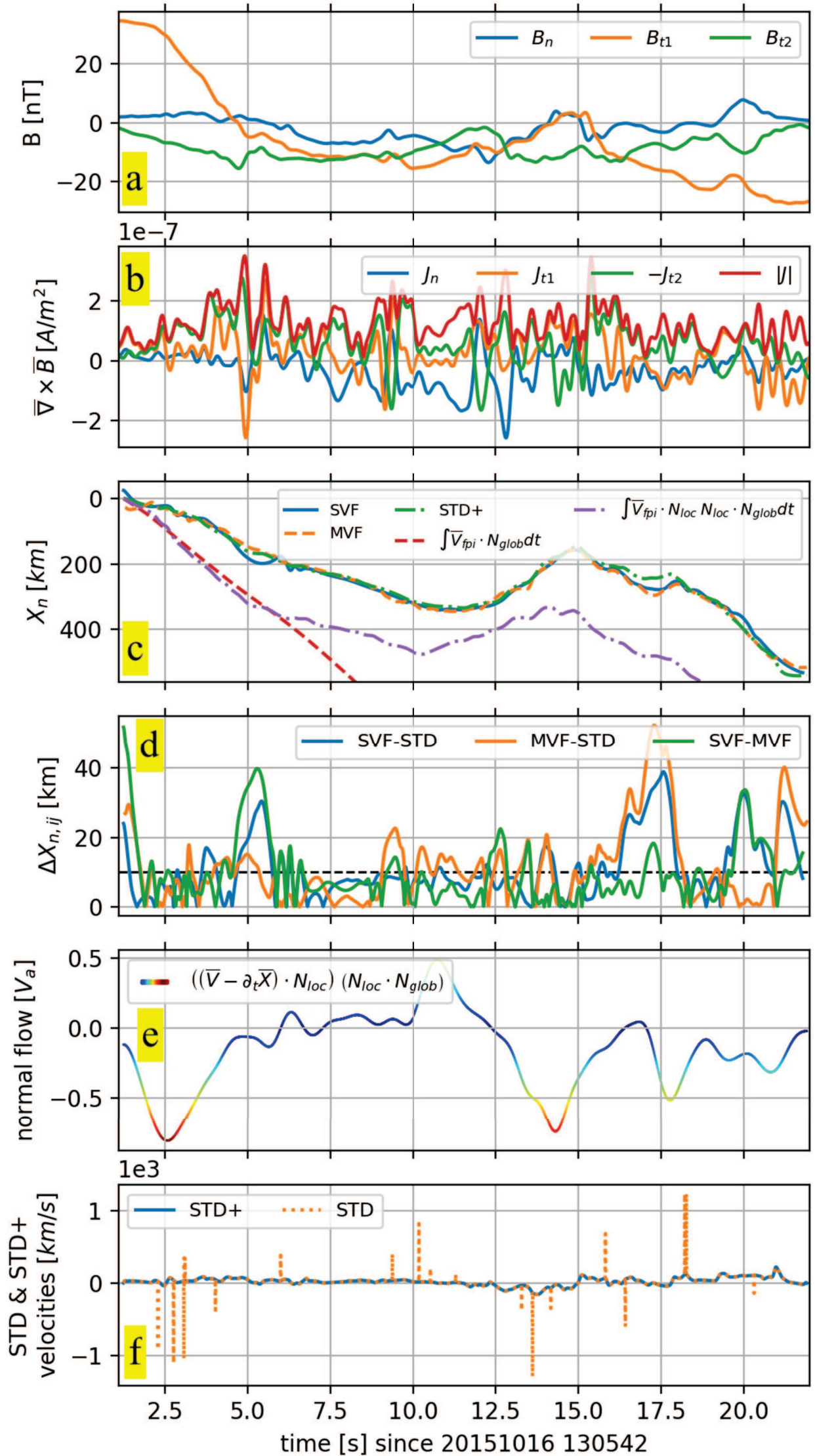
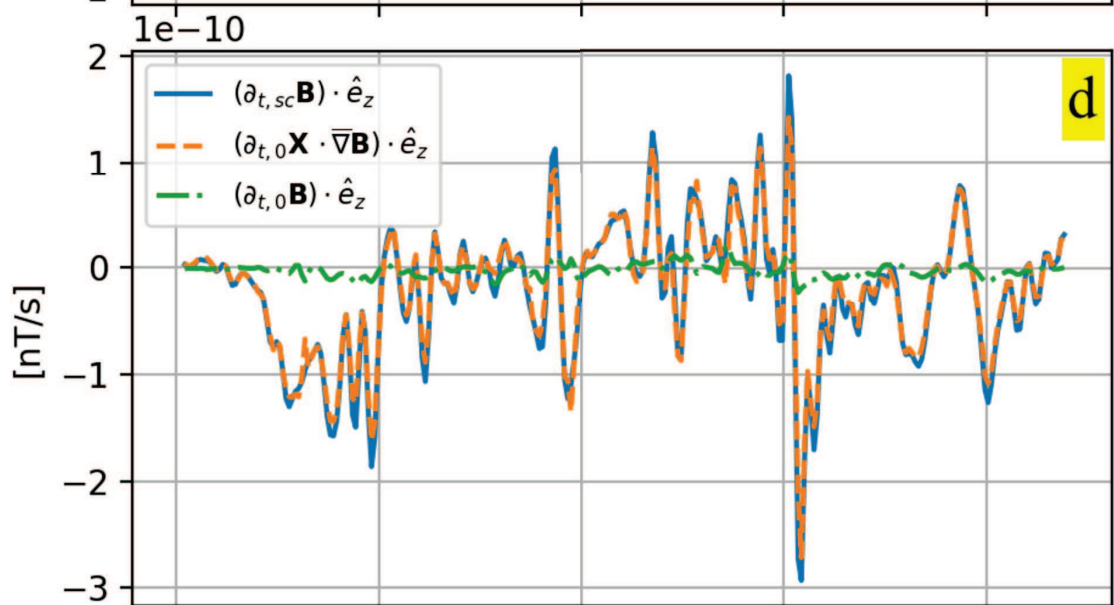
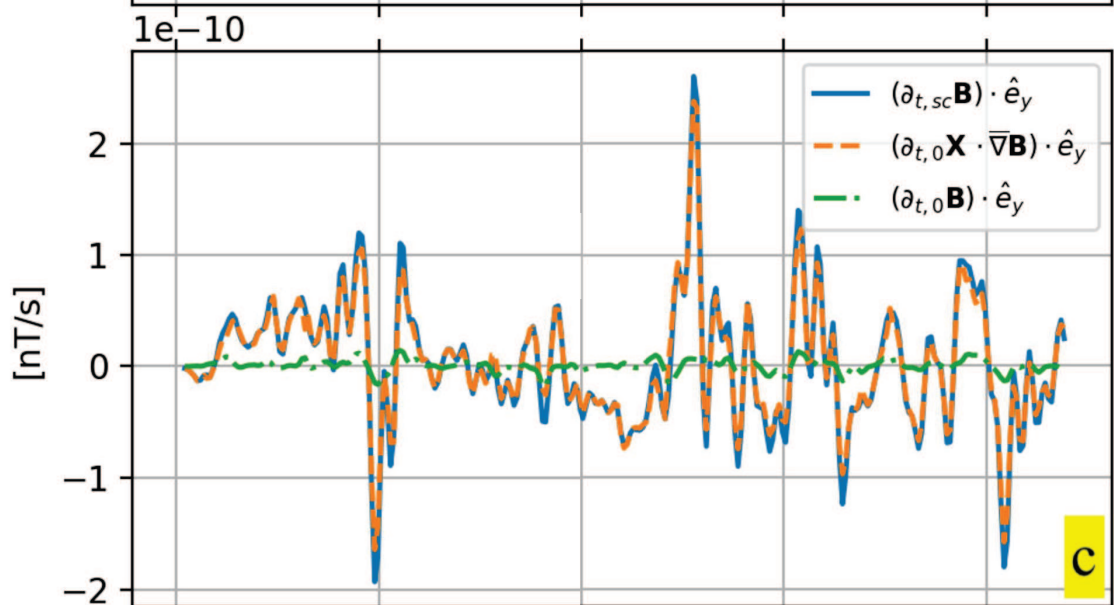
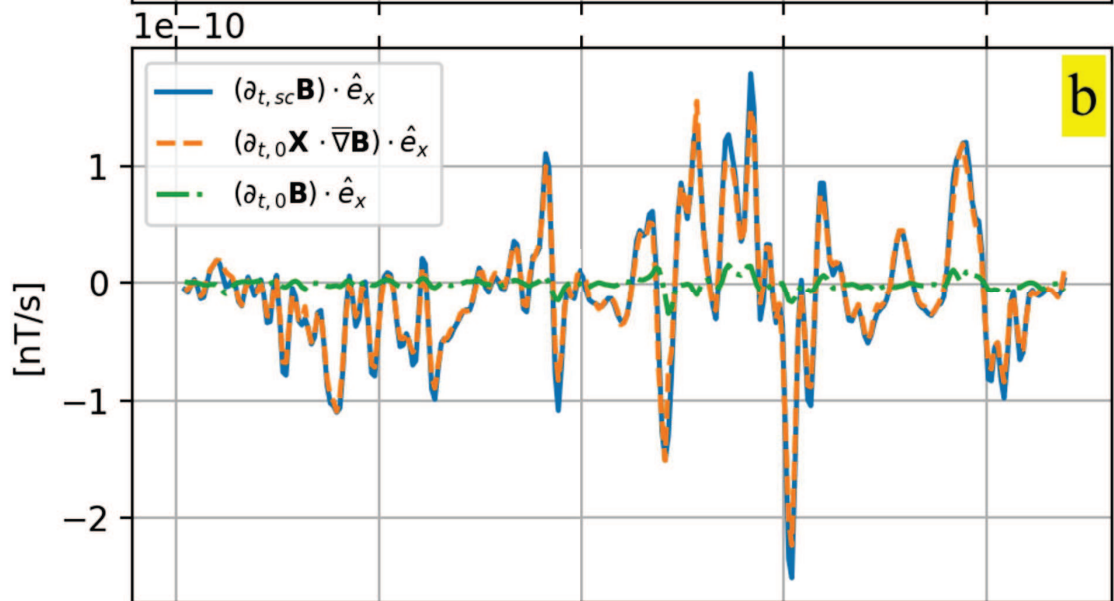
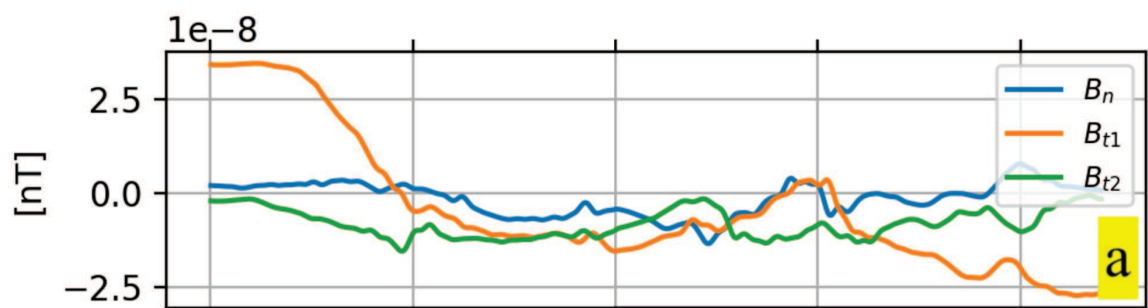


Figure7.



time [s] since 20151016 130542

Figure8.



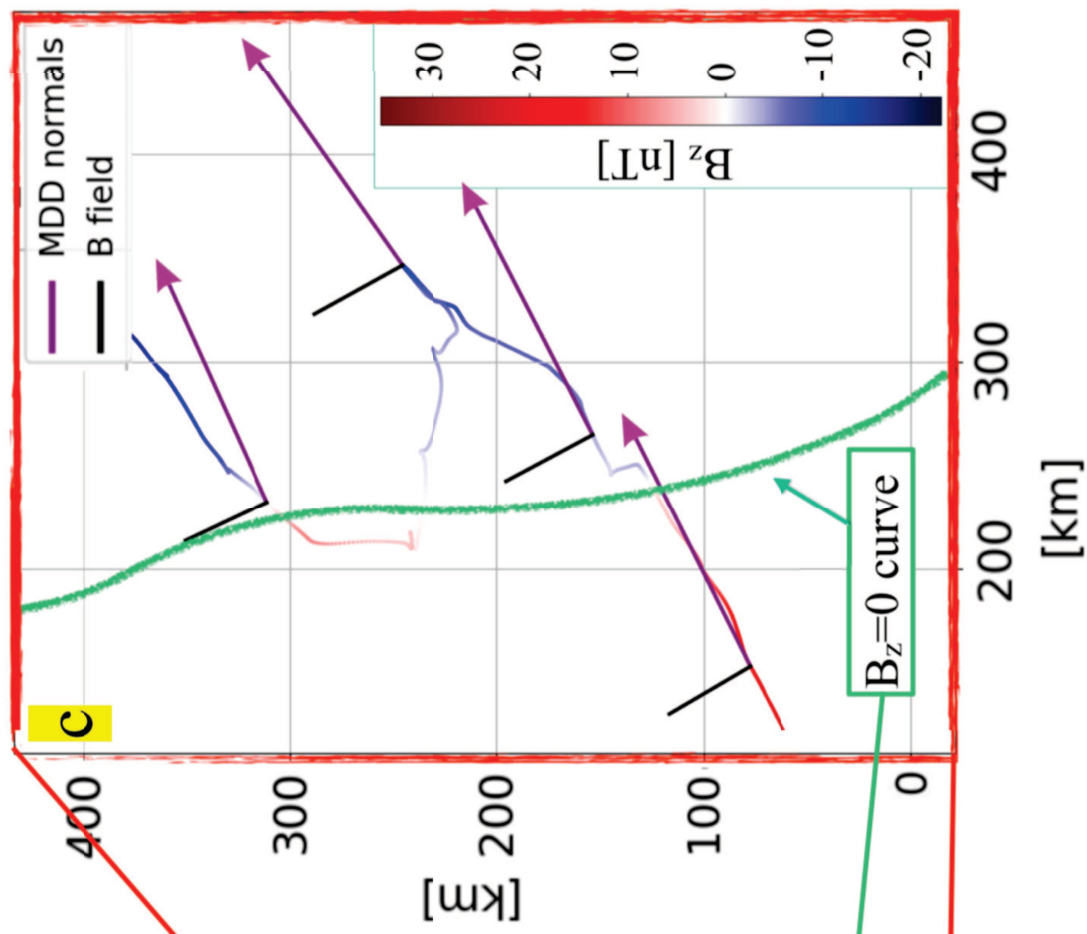
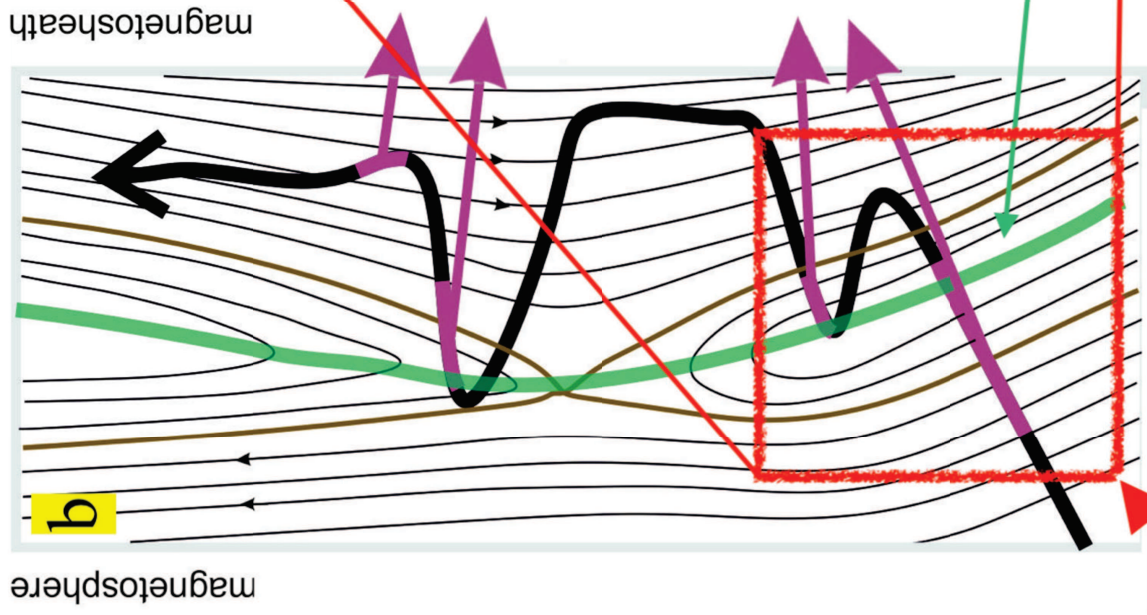
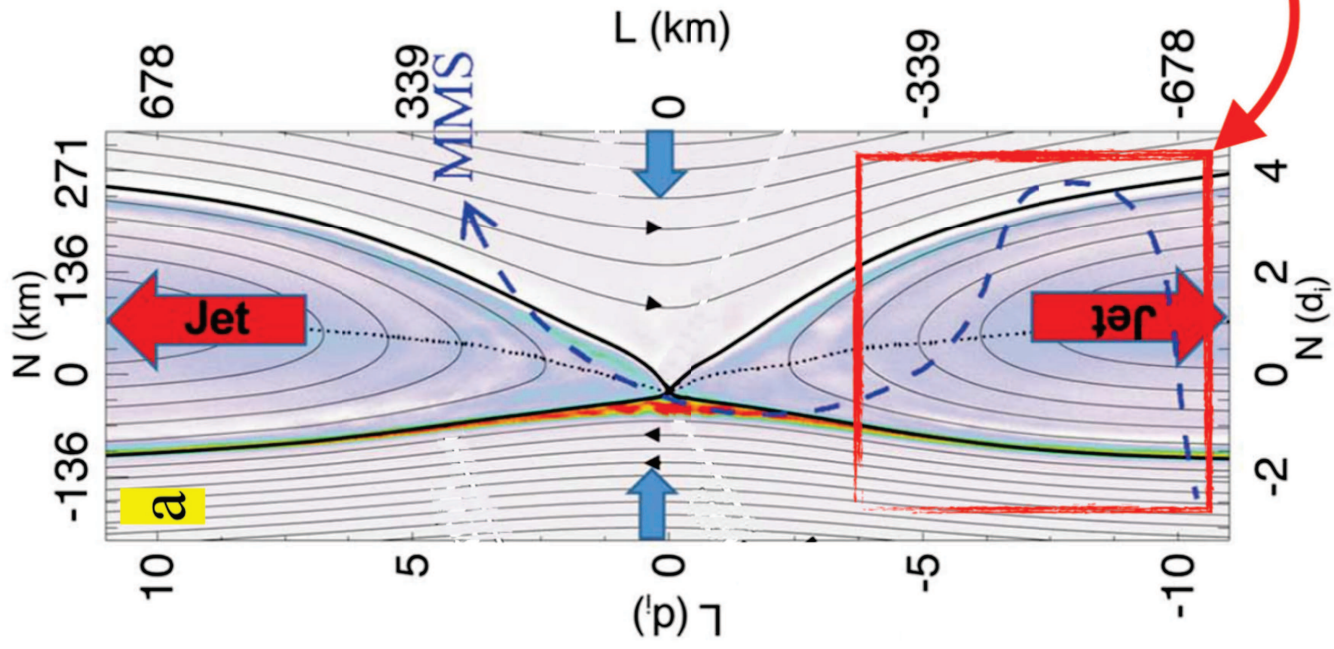
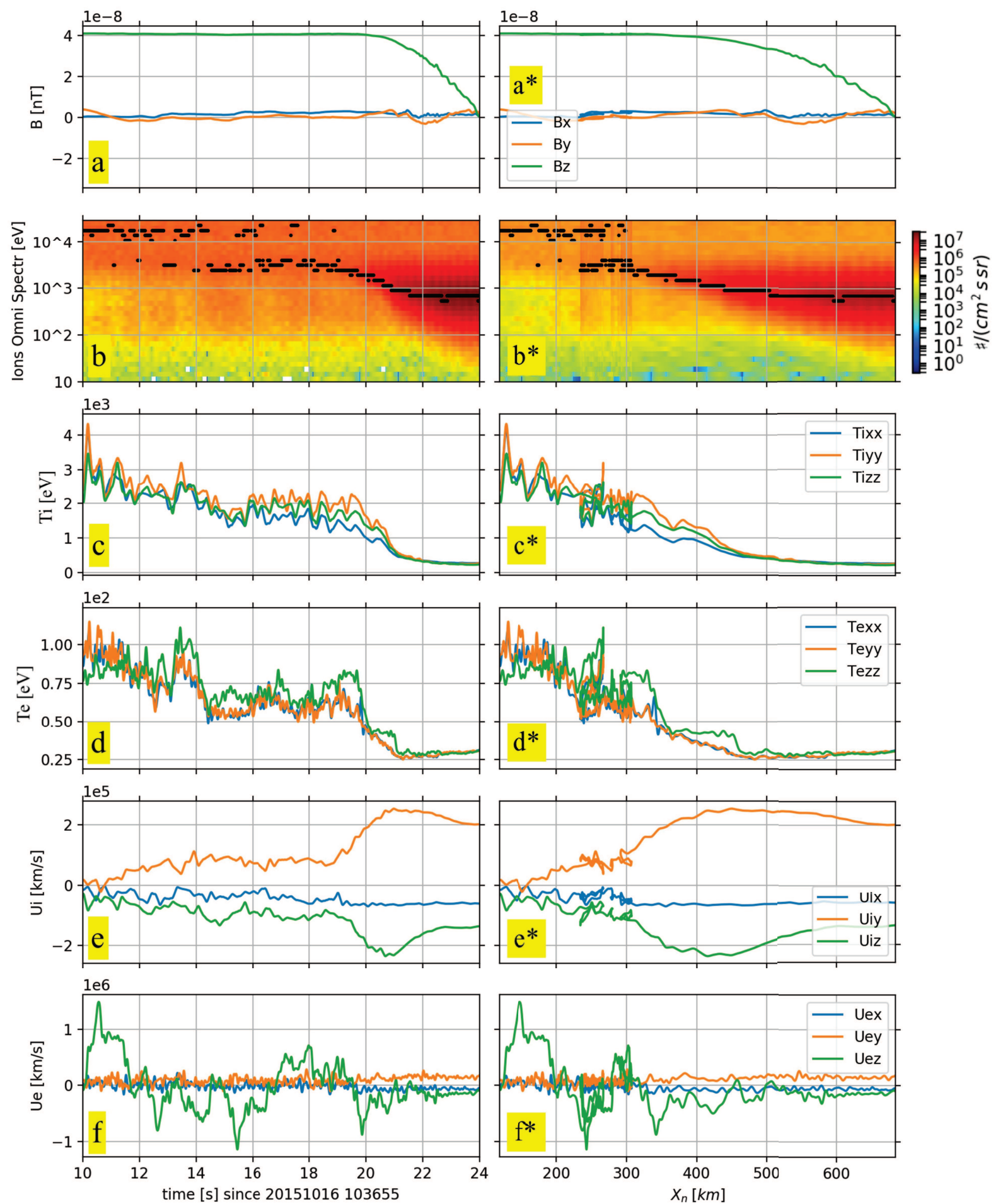


Figure9.





FigureA.1.

